

**LIPID BILAYER PERMEATION OF AN ALIPHATIC AMINE DRUG:
MODELING WITH MOLECULAR DYNAMICS SIMULATIONS AND KINETIC
RATE EQUATIONS**

by
TUĞÇE ORUÇ

Submitted to the Graduate School of Engineering and Natural Sciences
in partial fulfillment of
the requirements for the degree of
Master of Science

Sabancı University
June 2016

LIPID BILAYER PERMEATION OF AN ALIPHATIC AMINE DRUG:
MODELING WITH MOLECULAR DYNAMICS SIMULATIONS AND
KINETIC RATE EQUATIONS

APPROVED BY:

Asst. Prof. Dr. Deniz Sezer.....
(Thesis Supervisor)

Prof. Dr. Canan Atılgan.....

Assoc. Prof. Dr. Elif Özkırımlı Ölmez.....

DATE OF APPROVAL: 01/06/2016

© Tuğçe Oruç 2016

All Rights Reserved

ABSTRACT

LIPID BILAYER PERMEATION OF AN ALIPHATIC AMINE DRUG: MODELING WITH MOLECULAR DYNAMICS SIMULATIONS AND KINETIC RATE EQUATIONS

TUĞÇE ORUÇ

M.Sc. Thesis, June 2016

Supervisor: Asst. Prof. Dr. Deniz Sezer

Keywords: Aliphatic amines, drug permeation, lipid bilayer, molecular dynamics simulations, kinetic modeling

Aliphatic amine bearing drugs constitute about 27% of all orally active drugs. Since they comprise a large proportion, it is important to understand their permeation mechanism through cell membrane. In this thesis, the permeation of an aliphatic amine drug through a lipid bilayer is treated at three different levels of spatio-temporal resolution. On the finest scale, the interactions of the aliphatic amine drug dyclonine with the lipid bilayer are modeled in atomistic detail via molecular dynamics (MD) simulations. Because the aliphatic amine group is ionizable it can be in either positively charged or neutral. MD simulations reveal that both charge states penetrate into the bilayer and the neutral drugs easily translocate. However, complete permeation events are not observed. To understand the mechanism of permeation, therefore, a coarser model of one-dimensional diffusion in a potential is employed. To apply the model, diffusivity and free energy profiles along bilayer normal are obtained via MD simulations. The resulting hydrodynamic description of the permeation allows access to longer time scales and provides the calculation of the permeability coefficients. Finally, on the coarsest level, we model the drug permeation into liposomes via kinetic rate equations. The model reproduces recent experiments that measure the permeability coefficients of aliphatic amine drugs using pH-sensitive fluorophores. We observe that while the experimental assay is sensitive to the protonation rate of the drug, it is basically insensitive to the drug permeability. The multiscale modeling strategy employed here is very general and can be straightforwardly applied to other titratable drug molecules.

ÖZET

ALİFATİK AMİN İLACIN LİPİT İKİLİ KATMANINDAN GEÇİŞİ: MOLEKÜLER DİNAMİK SİMÜLASYONLARI VE KİNETİK HIZ DENKLEMLERİ İLE MODELLENMESİ

TUĞÇE ORUÇ

Yüksek Lisans Tezi, Haziran 2016

Danışman: Yard. Doç. Dr. Deniz Sezer

Anahtar kelimeler: Alifatik aminler, ilaç geçişi, lipit ikili katmanı, moleküler dinamik simülasyonları, kinetik modelleme

Alifatik amin içeren ilaçlar oral ilaçların %27'sini oluşturmaktadır. Büyük bir yüzdeye sahip oldukları için bu ilaçların hücre zarından geçiş mekanizmasını anlamak önemlidir. Bu tezde, alifatik amin içeren bir ilacın lipit ikili katmanından geçişi üç farklı uzamsal ve zamansal seviyelerde incelenmiştir. En küçük ölçekte, alifatik amin ilacın -dikloninin-lipit ikili katmanıyla olan ilişkisi moleküler dinamik (MD) simülasyonlarıyla atomik detayda modellenmiştir. Alifatik amin grubu iyonlaşabildiği için ilaç pozitif yüklü ya da nötr olabilir. Her iki yük durumunda da ilaçların ikili katmana girebildiği ve nötr ilacın kolaylıkla katman değiştirebildiği MD simülasyonları ile gösterilmiştir. Ancak, geçiş olayının tamamı gözlemlenmemiştir. Geçiş mekanizmasını anlamak için daha geniş ölçekli, potansiyel içinde bir boyutlu difüzyon modeli kullanılmıştır. Bu modeli uygulayabilmek için lipit ikili katmanı normal boyunca difüzyon ve serbest enerji profilleri MD simülasyonları ile oluşturulmuştur. Geçiş mekanizmasının hidrodinamik açıklaması daha uzun zamanlı olayların elde edilmesini ve geçiş sabitlerinin hesaplanmasını sağlamıştır. Son olarak, en kapsamlı boyutta, kinetik hız denklemleri ile lipozomlara ilaç geçişi modellenmiştir. Bu çalışma ile yakın zamanda gerçekleştirilmiş, pH değişimine hassas floroforlar kullanılarak lipozomlara alifatik amin geçişini ölçen deneyler modellenmiştir. Bu model ile deneysel sistemin ilacın proton alma hızına hassas olduğunu, ilaç geçişine ise duyarsız olduğunu gözlemlemekteyiz. Bu çalışmada uygulanan çok ölçekli modelleme stratejisi oldukça geneldir ve diğer iyonlaşabilen ilaçlar için kolay bir şekilde uygulanabilir.

To ones who taught love and laugh

Acknowledgements

First of all, I would like to thank to my supervisor Deniz Sezer even though I know it is never enough to thank him. All the works presented in this thesis were completed thanks to his infinite desire to teach. It was not generally easy for me to perceive how I should do the necessary work, but each time he explained the concepts and what I am supposed to do in detail with a great patience. Therefore, I feel so lucky that I had opportunity to study under his supervision for two and a half years.

I want to thank to Canan Atılgan and Elif Özkirimli Ölmez for accepting to be in my thesis jury and their valuable contributions. I also want to thank to Murat Çokol for both introducing us the molecules that I studied and allowing me to use his laboratory whenever I wanted.

Additionally, I would like to thank to all my family for supporting me in each step of my life. I was so lucky that I grew up with three mothers and two fathers. Therefore besides thanking to my mother Güldal Oruç, my father Abdullah Oruç and my sister Hande Kırmızı; I specifically want to thank to my grandmothers Yücel Uyar, Semahat Oruç and my grandfather Eşref Oruç. Even though my grandparents are not physically with me any more, it is priceless to have their love in my heart in every second of my life.

Everything is meaningful and valuable as long as we are lucky enough to have people we love around us. I was extremely lucky that I became a member of G022 in which I think I gained lifelong friendships. All my friends in Sabancı University are so important to me, but I specifically want to thank to Aslı Yenenler, Anı Akpınar, Esra Sinoplu and Ahmet Sinan Yavuz for making it extremely difficult to me to leave Sabancı University.

Contents

1	Introduction and Motivation	1
1.1	Drugs and Synergy	1
1.1.1	Measurement of Drug Efficacy	1
1.1.2	Measurement of Drug Synergy	3
1.1.3	Systematic Exploration of Pairwise Drug Synergies	4
1.1.4	Mechanism of Synergy	5
1.2	Physicochemical Properties of Drugs	5
1.3	Scope of the Thesis	7
2	Dyclonine - Lipid Bilayer Interactions: Molecular Dynamics Simulations	9
2.1	Methods	9
2.1.1	Parametrization of Dyclonine	9
2.1.2	Construction of Pure Lipid Bilayer	11
2.2	Results	12
2.2.1	Charged Dyclonine	12
2.2.2	Neutral Dyclonine	15
2.2.3	Neutral Dyclonine Inside the Bilayer	17
2.3	Discussion	22
3	Permeability from MD simulations	24
3.1	Theory and Methods	24
3.1.1	Diffusion Equation and Permeability	24
3.1.2	Free Energy Profiles from Umbrella Sampling Simulations	25
3.1.3	Local Estimate of Diffusion	27
3.1.4	Global Estimate of Diffusion Profile	30
3.1.5	Permeation in Three Layers	38
3.2	Results	39
3.2.1	Free Energy Profiles	39
3.2.2	Diffusion Profile	43
3.2.3	Permeation	47
3.3	Discussion	48

4	Modeling Experimental Studies in Drug Permeation	51
4.1	Introduction	51
4.2	Methods	53
4.3	Results	56
4.4	Discussion	63
5	Conclusion and Outlook	64
5.1	Conclusion	64
5.2	Outlook	65

List of Figures

1.1	Dose-response curves of dyclonine treated yeast cells	2
1.2	Dose-response curves of pentamidine treated yeast cells	2
1.3	Interaction experiment of dyclonine and pentamidine	3
1.4	Synergistic drug pairs reported at Cokol et al.	4
1.5	Drug classification based on their charged state reported at Manallack et al.	6
1.6	Structure of charged and neutral dyclonine.	8
2.1	Fragments of dyclonine used for determination of energy parameters.	10
2.2	Energy profiles of fragment 1 with respect to dihedral χ_1	10
2.3	Energy profiles of fragment 2 with respect to χ_2 and χ_3	11
2.4	Four configurations of dyclonine molecule	11
2.5	χ_1 , χ_2 and χ_3 distribution in 10 ns simulations	12
2.6	Charged Dyclonine initial and final view	13
2.7	Localization of charged dyclonine molecules	14
2.8	Successful insertion of dyclonine into lipid bilayer	14
2.9	Unsuccessful insertion of dyclonine into lipid bilayer	15
2.10	Tilt angle of dyclonine	15
2.11	Orientation of charged dyclonine molecules	16
2.12	Neutral dyclonine initial and final view	17
2.13	Localization of neutral dyclonine molecules	18
2.14	Insertion of dyclonine into lipid bilayer	18
2.15	Orientation of neutral dyclonine molecules	19
2.16	Clustering of neutral molecules in aqueous environment	19
2.17	Initial and final view of 4D ⁰ system	20
2.18	Localization of neutral dyclonine molecules in double bilayer	20
2.19	Orientation of neutral dyclonine molecules in double bilayer	21
2.20	Mechanism of translocation	21
3.1	Initial view of umbrella sampling systems for windows $ z = 4, 2.1$ and 1.1 nm	26
3.2	Initial view of umbrella sampling systems for window $ z = 6$ nm	26

3.3	Position distributions of all windows for umbrella sampling simulations	28
3.4	pTCFs of D^+ and D^0 in aqueous environment	28
3.5	pTCFs of D^+ and D^0 at the center of the bilayer	29
3.6	Errors of D^+ and D^0 along reaction coordinate	30
3.7	Diffusion coefficients of D^+ and D^0 for all exponential fits	30
3.8	Regions of simulation box for calculation of diffusion profile via global estimate	32
3.9	$T_{x \leftarrow}^{<xb }(z)$ and $T_{z \rightarrow}^{ az>}(x)$ profiles	32
3.10	$T_{x \rightleftharpoons}^{ ab }(z)$ and diffusion profiles	33
3.11	$T_{x \rightarrow}^{ ax>}(z)$ and $T_{z \leftarrow}^{<zb }(x)$ profiles	34
3.12	$T_{\rightleftharpoons x}^{ ab }(z)$ and diffusion profiles	34
3.13	Diffusion profiles with different boundaries	35
3.14	Determination of round trip time for region II	35
3.15	Determination of round trip time for region II	36
3.16	Determination of round trip time for region IV	37
3.17	Determination of round trip time for region IV	37
3.18	Free energy profiles of dyclonine molecules in $8D^+$, $8D^0$ and $4D^0$ systems	40
3.19	Energy profiles of charged and neutral dyclonine from unrestrained and restrained simulations	41
3.20	Free energy profiles with different simulation times	42
3.21	Number of phosphorous atoms and water molecules in core region of the lipid bilayer	42
3.22	View of lipid bilayer while charged and neutral dyclonine molecules are located at the center	43
3.23	Diffusion profiles determined via global approach for selected intervals	44
3.24	Diffusion profiles of dyclonine with both global and local approaches	45
3.25	τ_{rt} calculated from fitted diffusion function consistent with τ_{rt} determined MD simulations	46
4.1	pH change over time for <i>model 1a</i>	57
4.2	Drug concentration change over time for <i>model 1a</i>	57
4.3	pH and neutral drug concentration profiles when neutral drug concentration is kept constant	58
4.4	Effects of fluorescence molecule on pH profile	59
4.5	Impacts of charged drug and proton permeation into the vesicle	59
4.6	Blockage of charged drug permeation via introducing membrane potential	60
4.7	Addition of ions to the system impacts membrane potential	60
4.8	Effect of k_{on} on k_a	61
4.9	<i>Model 2b</i> in longer time scale	62

4.10 Effect of permeability coefficients of ions on pH profile for longer time scale	62
---	----

List of Tables

2.1	Dihedral angles of dyclonine’s four conformations.	10
3.1	Harmonic force constants (k) and total simulation time (T) for corresponding restraining positions (z) of the umbrella potentials.	27
3.2	Fragments of reaction coordinate separated by virtual boundaries for estimation of τ_{rt}	32
3.3	Calculated permeability coefficients (cm/s) for charged and neutral dyclonine with different choice of borders	47
3.4	Calculated “resistances” (per nm) to the insertion into, translocation through, and dissociation from a DPPC lipid bilayer.	47
4.1	Coefficients of fitted four exponential function to fluorescence signal of propranolol.	53
4.2	Parameters used in the model.	53
4.3	Coefficients of biexponential fits to simulations of different \mathcal{P}_{D^0}	61
4.4	Coefficients of biexponential fits to simulations of different k_{on}	61

Chapter 1

Introduction and Motivation

1.1 Drugs and Synergy

1.1.1 Measurement of Drug Efficacy

Drugs can be defined as chemical substances that have any effect on any living organism. In medicine, they are used for many purposes including diagnosis, treatment and cure of a disease. The number of drugs increases day by day and the total amount of drugs as of May 2016 is 8206 [1].

Drugs should have an effect on the phenotype of a selected organism. For unicellular organisms, a measure of the effect of a drug can be the change in the growth curve of the organism. The growth curve shows how the number of cells in a population changes over time. In the case of cells that grow in an aqueous environment, the concentration of cells in a given compartment can be measured by monitoring the optical density (OD) of the solution. As it is seen in the first box of Figure 1.1, OD_{600} value (optical density, the measure of the concentration of the cells) changes over time. Here, we see how the concentration of *Saccharomyces cerevisiae* is changed in 18 hours. In approximately first ten hours no increase in the curve is observed which is called lag phase. Afterwards, the OD_{600} value increases indicating that the population of cells grows steadily. This phase is either called logarithmic (log) or exponential phase. Finally, the concentration of the cells reaches a stationary phase which is barely seen in the figure. Drugs may exhibit their impact by affecting any of these phases, or more than one phase simultaneously.

For example, the drug dyclonine has an effect on yeast cells through targeting an ergosterol pathway protein Erg2 [2]. This effect can be observed in yeast cells in a dose-dependent manner. Figure 1.1 shows the results of the experiments that I conducted by subjecting yeast cells to increasing doses of dyclonine. How yeast populations respond to linearly increased dosage of dyclonine (dyc) is seen in the figure. While in the first box, no drug was given to the yeast cells, in the last box the minimum inhibitory concentration (MIC) of the drug was applied. As the concentration of the drug increases, the lag time

of the growth curves elongates. Therefore we can conclude that dyclonine affects the lag phase in a dose-dependent manner. For simplicity, let me define the “growth” as the total area under the growth curve. For larger drug concentrations the area under the growth curve decreases.

Meanwhile, we were ought to see maximum effect in the 7x concentration that corresponds to minimum inhibitory concentration (MIC, which corresponds to $50 \mu\text{M}$ in this case) in which no growth should be detected. However, there must be an experimental error resulting an increase in the concentration of the cells.

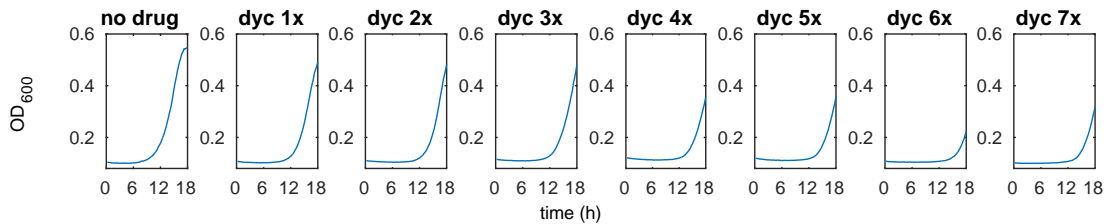


Figure 1.1: Growth curves of yeast cells in the presence of dyclonine with linearly increased dosage (from left to right) is shown. Increase in dosage of dyclonine cause a decrease in the “growth” of the yeast cells. At first box, no drug was applied to cells and at last box (7x) minimum inhibitory concentration of drug was applied.

Pentamidine offers another example of a drug which is effective on yeast cells. Figure 1.2 shows the results of the experiments that I conducted by subjecting yeast cells to increasing doses of pentamidine. We again see that as the concentration of the drug increases (from no drug to MIC which is $100 \mu\text{M}$ in this case), the slope of the exponential growth phase decreases. Since this slope is related to the growth rate we can conclude that pentamidine affects the growth rate in a dose-dependent manner; namely as the dosage of the drug increases, the growth rate of the cell decreases.

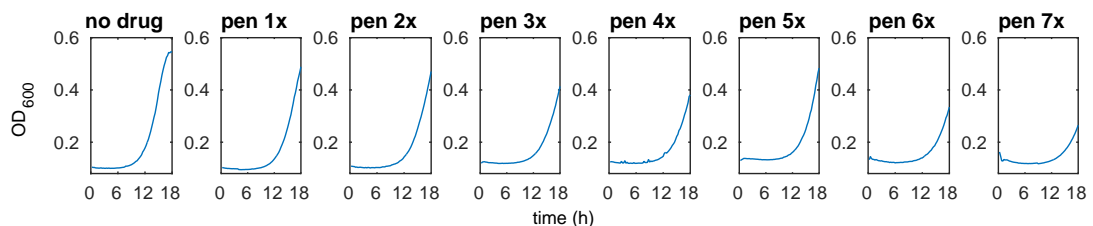


Figure 1.2: Growth curves of yeast cells in the presence of pentamidine with linearly increased dosage (from left to right) is shown. Increase in dosage of pentamidine cause a decrease in the “growth” of the yeast cells. At first box, no drug was applied to cells and at last box (7x) minimum inhibitory concentration of drug was applied.

Note that dyclonine and pentamidine are just two of the drugs in the market. Actually, there are enormous number of drugs and it is never sufficient to cure all diseases. While constitution of new therapeutic drugs is a way to obtain more effective results in treat-

ment, combining current drugs to obtain synergistic outcomes is another possibility that is extensively studied in pharmaceutical research [3].

1.1.2 Measurement of Drug Synergy

If the combination of at least two drugs shows an effect that is “better” than their individual outcome, then these drugs are called synergistic. For instance, in Figure 1.1 we see maximum effect (minimum growth) of dyclonine in the 7th box and in Figure 1.2 we see maximum effect (minimum growth) in 8th box, which means in order to see the effects of drugs we should use at least 6x and 7x concentrations, respectively. When these two drugs are used together if we see less growth than their individual maximum effect, then these two drugs are called synergistic. In Figure 1.3, results of an interaction experiment of dyclonine and pentamidine is shown. This experiment was performed in order to see whether these two drugs are synergistic or not. In horizontal axis dosage of dyclonine, in vertical axis dosage of pentamidine were increased. At the bottom left corner, no drug was applied to the cells.

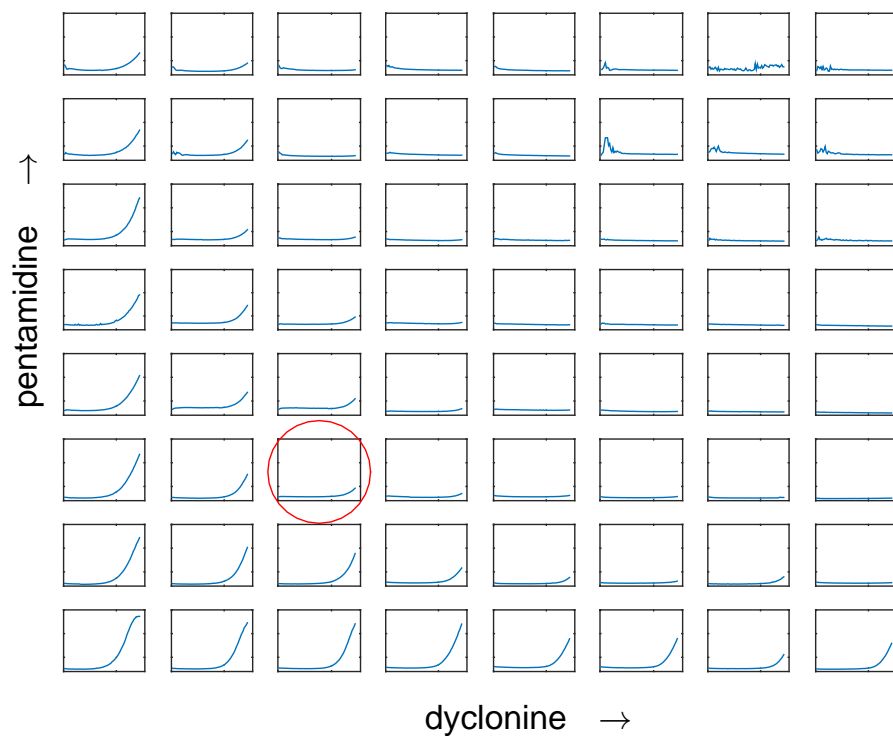


Figure 1.3: Interaction experiment was performed for dyclonine and pentamidine in order to determine the synergistic effects of the drugs. In horizontal axis, concentration of dyclonine was linearly increased and in vertical axis, concentration of pentamidine was linearly increased. Red circle shows the box in which 2x concentrations of each drugs are present.

Lets focus to the box in which 2x of both drugs were treated. It is shown in the red circle of Figure 1.3. It is seen that in that box “growth” of the cells are clearly less than 7x

dosage of pentamidine and slightly lower than 6x dosage of dyclonine. Note that in that well there is 4x dosage of drug in total which is less than individual dosages of dyclonine and pentamidine 6x and 7x, respectively. Therefore, as less dosage of drugs in total is more “effective” than individual dosages, these drugs (dyclonine and pentamidine) are synergistic with each other.

One important advantage of drug synergy is the fact that side effects of the synergistic drugs do not show synergy usually. Therefore, revealing new drug pairs and understanding the mechanism of the synergy has become a widely studied area. [3].

1.1.3 Systematic Exploration of Pairwise Drug Synergies

As drug synergy is vital for new treatments, systematic investigation of synergistic drug pairs constitutes an important research area. Cokol et al. studied whether a set of drugs (including dyclonine and pentamidine) have synergistic interactions with each other on the yeast cells. In Figure 1.4, at left panel we see results of interaction experiments. Note that each interaction experiment has 8×8 matrix which actually represent Figure 1.3 like matrix in colormap view. White boxes indicate maximum growth which scales down via shades of red to black boxes which means no growth. As a result, they indicate synergistic pairs with a green “S”. Note that there are red “A” in some boxes which indicates antagonistic interaction of corresponding drug pairs. Antagonistic drugs repress each others activity on the contrary of synergy. It is seen that pentamidine and terbinafine have the maximum number of pairs. In the right panel of the same figure drugs are connected to each other based on their interaction type. Importance of “promiscuous synergizers” will be discussed in the following section.

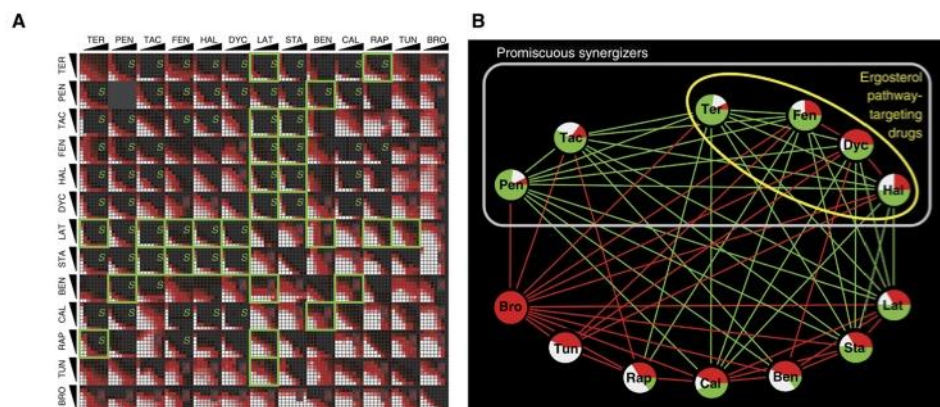


Figure 1.4: (A) Growth of yeast with different drug exposure increasing to minimum inhibitory concentration of each drug. S and A indicate synergistic and antagonistic interaction, respectively. Green squares shows the drug pairs which target proteins expressed by synergistic genes. (B) Interaction of drug pairs. Green and red lines show synergy and antagonism respectively. “Promiscuous synergizers” are shown in rectangle which have highest number of synergistic pairs. Figure is taken from Ref. [3].

1.1.4 Mechanism of Synergy

Different proteins on different pathways may be responsible for a specific phenotype in living organisms. These related pathways are called parallel pathways. If two drugs target two different proteins in these parallel pathways, then synergistic effect on the phenotype can be observed. This is one possible mechanism of synergy. In that case these genes encoding the targeted proteins have synergistic genetic interaction.

Another possible mechanism for drug synergy is that a drug can increase the bioavailability of another drug which results synergism.

Cokol et al., have tested drugs which target parallel pathways that have synergistic genetic interactions. Each drug targets a different protein in a known synergistic genetic interaction (with an exception of ergosterol pathway). As a result, they observed that all interactions cannot be explained via synergistic genetic interaction especially for the ones grouped as “promiscuous synergizers”. In addition to experiments performed with these dataset, more experiments were conducted for pen, ter and tac with drugs whose targets do not have genetic interactions with their targets. Results supported the promiscuity of the aforementioned drugs which reinforced the idea that synergistic interactions for promiscuous synergizers are caused by some other reason rather than genetic interactions of the targeted proteins [3]. This situation raises the possibility of increment of bioavailability mechanism.

One of the possible ways to increase the bioavailability of a drug is to ease its permeation through the cell membrane which leads an elevation in the number of drugs that can reach their target inside of the cell. Therefore one possible bioavailability mechanism for drug synergy is the situation in which two drugs may “help” each other while passing through cellular membrane.

The ability of permeation of a drug though lipid bilayer actually depends on its physicochemical properties rather than its biological activities.

1.2 Physicochemical Properties of Drugs

For a drug to be able to penetrate into the bilayer, first it should have a tendency to localize in hydrophobic environment. The measure of this tendency is the lipophilicity of the drug which is basically lipid-likeness. Lipid-likeness of a molecule is measured by the partition coefficient which is determined as

$$P = \frac{[Drug]_{octanol}}{[Drug]_{water}}, \quad (1.1)$$

when the drug is in its neutral state.

For drug-likeness, lipophilicity of a compound should be in a critical range. For example, according to Lipinski’s rule of five (which is widely accepted approach in deter-

mination of drug-likeness), logP (base 10 logarithm of the partition coefficient) values should be smaller than five [4]. Another study that has classified drugs based on their logP values, indicates distribution gives the peak at around logP = 2.5-3 [5].

Meanwhile, in another study of Cokol group, they show that synergicity and lipophilicity are positively correlated [6]. It is seen that besides being a determinant factor in drug-likeness, lipophilicity is also important in other properties like synergy.

Recent study performed by Manallack et al. analyzed the charged states of the drugs [7] classified them based on their ionizability as it is shown in Figure 1.5. Results showed that single basic drugs comprise the highest proportion, 27.8%, of all drugs (note that this is even larger than proportion of the neutral drugs). Besides, single acidic drugs have a portion of 14.2%. Additionally, always ionized groups are only 6.3% of all drugs.

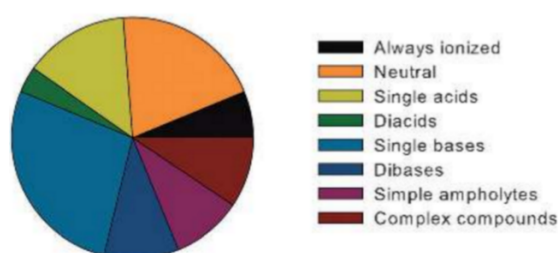


Figure 1.5: single drugs have the highest proportion which is even larger than neutral drugs. Single acidic drugs have also large proportion which is slightly smaller than neutral drugs. Meanwhile always ionized drugs have second smallest proportion. These ratios suggest that bearing a charged group is a preferred condition. Figure is taken from Ref. [7].

In addition to classification of the drugs based on their charged state, they also analyzed and discriminated the drugs depending on the type of functional groups. They noticed that among all functional groups aliphatic amines comprise the ratio of 27.1% and the ratio of carboxylic acids is 20.1%. Among aliphatic amines, the proportion of tertiary amines is 49% [8]. On the other hand, same research group also scanned non-drug small compounds and performed same classification for these compounds. They showed that aliphatic amine ratio is only 3.4% among non-drug substances, similarly ratio of carboxylic acids is only 2.4% [7]. These results emphasize two points: (i) single ionizable group bearing drugs constitute more than half of the drugs, (ii) among these ionizable groups some functional groups are more abundant (aliphatic amines for basic drugs and carboxylic acids for acidic drugs) and having these ionizable groups is a determinant factor to be a drug or not.

Note that while bearing a charged group is an advantage for a molecule to be a drug, having it permanently is not a preferred condition (since their ratio is only 6.3%). Besides the probability of affecting other properties like distribution and metabolism, having permanent charge may reduce the success of permeation through lipid bilayer since ionic

components need to overcome a high energy barrier. This situation brings pK_a of drugs into the stage. pK_a , acid dissociation constant, can be described as



where AH is an acidic substance with dissociation constant, K_a in which

$$K_a = \frac{[A^-][H^+]}{[AH]}. \quad (1.3)$$

As we take logarithm of both sides on base 10,

$$\log_{10}(K_a) = \log_{10} \frac{[A^-]}{[AH]} + \log_{10}[H^+]. \quad (1.4)$$

Since pH is $-\log_{10}[H^+]$ and pK_a is $-\log_{10}(K_a)$,

$$pK_a = -\log_{10} \frac{[A^-]}{[AH]} + pH. \quad (1.5)$$

Therefore, the ratio of two charged state of a compound can be denoted as,

$$\frac{[A^-]}{[AH]} = 10^{pH-pK_a}. \quad (1.6)$$

Similarly for a basic substance,

$$\frac{[B^+]}{[BH]} = 10^{pK_a-pH}. \quad (1.7)$$

In other words, pK_a is a decisive property for charged state and abundance of the state in a certain environment (specific pH). In the same study, Manallack et al. also evaluated the pK_a of single basic and single acidic drugs [7]. They report that more than half of the basic drugs have pK_a between 8-10 and approximately half of the acidic drugs have pK_a between 3-5.

When we analyze the structure of the drugs that are synergistic pair with pentamidine, we see that most of them bear an aliphatic amine group.

1.3 Scope of the Thesis

As all synergistic pairs of pentamidine have aliphatic amine group, understanding the mechanism of how aliphatic amine bearing drugs permeate through lipid bilayer is a intriguing issue. Since aliphatic amines comprise substantially high proportion of drugs based on their functional groups, studying dyclonine which is an ionizable tertiary aliphatic amine bearing drug with pK_a 8.4, $\log P$ 3.68 [9] may provide an explanation for permeation mechanism of most of the drugs.

As dyclonine has an ionizable amine it can be in both charged and neutral states depending on the pH of the environment.

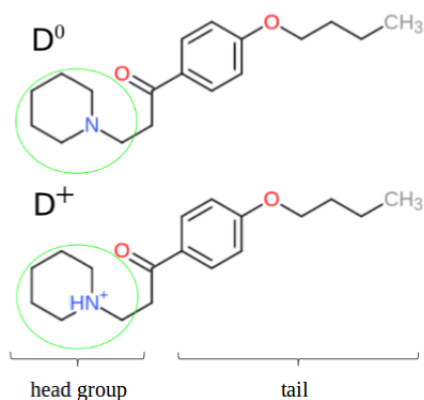


Figure 1.6: Dyclonine molecules can be both neutral and charged states. Aliphatic amine ring is shown in green circle. Circled group is defined as “head group” and the rest is defined as the “tail” of the molecule.

Dyclonine has different targets in different organisms. It was shown that dyclonine has antibacterial and antifungal effects [10]. Moreover, dyclonine is used as local anesthetic since it diffuses across the bilayer and binds to the inner pore of ion channels, resulting in inhibition of ion transport of nerve cells [11]. Note that the permeation mechanism of local anesthetics through the lipid bilayer is another area that is widely studied both experimentally and computationally [12, 13, 14, 15].

In this research it was aimed to understand the permeation mechanism of dyclonine through lipid bilayer via molecular dynamics simulations. For this purpose, characteristic behaviors of dyclonine - lipid interactions and permeation process with “three-layer” perspective are studied for both charge states of the molecule. Additionally, an experimental method which is used to determine permeability coefficients of drugs is modeled via kinetic rate equations with an increasing complexity.

Chapter 2

Dyclonine - Lipid Bilayer Interactions: Molecular Dynamics Simulations

2.1 Methods

2.1.1 Parametrization of Dyclonine

To perform molecular dynamics (MD) simulations of dyclonine it is necessary to construct force field parameters for both the neutral and charged states of the molecule (Figure 1.6). We first constructed the neutral state and achieved charged state by simply adding hydrogen atom. Therefore building neutral state is explained in detail in this section. In order to obtain three dimensional structure of dyclonine, energy parameters of neutral state was determined by splitting the molecule into two fragments as it is shown in Figure 2.1.

Topology files were constructed for two fragments separately. Initial parameters of the fragments and partial charges of atoms were determined via using similar structures which are already found in the Charmm36 force field ([16, 17, 18]). Since this led us to determine most of the parameters but not all, *ab initio* calculations were performed to determine the correct configurations of both fragments. By using Gaussian software [19] one dihedral angle (Figure 2.1 atoms of CA, ND, CM2 and CM1 - χ_1 - of fragment 1 and two dihedral angles (Figure 2.1 atoms of CG CX CM1 CM2 and CD1 CG CX CM1 - χ_2 and χ_3 of fragment 2 were scanned with 15 degree intervals. Resulting energy values of corresponding dihedral angles were obtained by adjustment of parameters with structural and vibrational analysis.

In Figure 2.2, we see the energy values of conformations with corresponding dihedral angles for the fragment 1. It is seen that energy profile of conformations constructed by adjustment of parameters by Charmm (black) is highly similar to the energy profile obtained by Gaussian (red). This shows that determined energy parameters of Charmm are successful enough as it mimics *ab initio* calculations. In the figure, we see there is

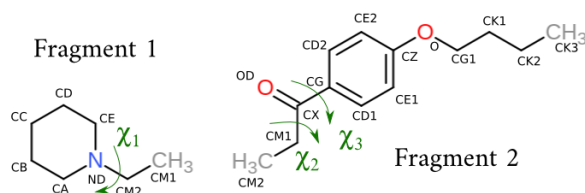


Figure 2.1: Determination of three dimensional structure was performed by splitting the molecule into two fragments. In fragment 1 one dihedral angle, χ_1 , and in fragment 1 two dihedral angles, χ_2 and χ_3 are scanned with 15° intervals.

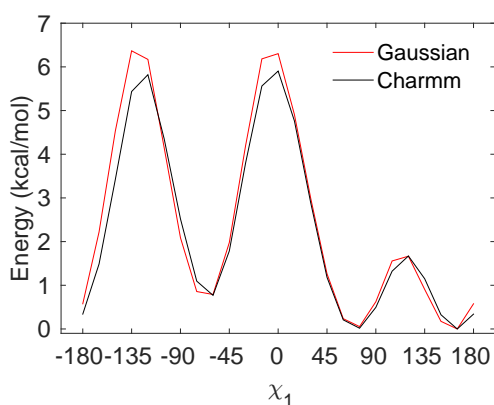


Figure 2.2: Energy profiles for fragment 1 is shown with respect to dihedral angle of dihedral χ_1 . Energy values are determined via Gaussian (red) and Chamm (black) after adjustment of energy parameters are shown.

three local minima whose corresponding dihedral angles (which are -70° , 70° and 165°) provide preferred conformations. Dihedral angles of -70 and 70 were selected for initial conformations of this fragment.

Similarly, in Figure 2.3, we see the energy values for fragment 2 that were obtained via Gaussian (red) and by adjusting charmm parameters (black). Since local minimum values are located at where dihedral χ_3 is either 0° or 180° and χ_2 is 180° , these dihedral angles were selected for initial conformations of fragment 2.

Eventually, we ended up with four conformations (Figure 2.4). Dihedral angles of each conformation is given in Table 2.1.

	χ_1	χ_2	χ_3
C ₁	70°	180°	180°
C ₂	-70°	180°	180°
C ₃	70°	180°	0°
C ₄	-70°	180°	0°

Table 2.1: Dihedral angles of dyclonine's four conformations.

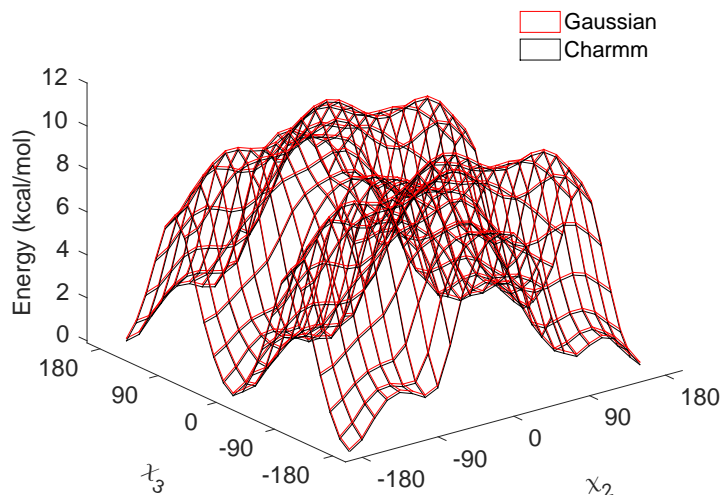


Figure 2.3: Energy profiles for fragment 2 is shown with respect to dihedrals χ_2 and χ_3 . Energy values are determined via Gaussian (red) and Charmm (black) after adjustment of energy parameters are shown.

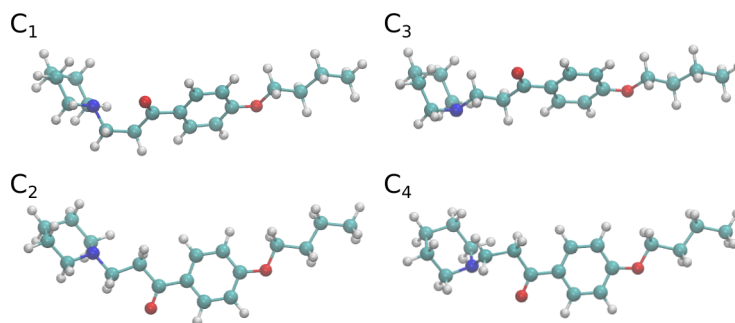


Figure 2.4: After determination of energy parameters of both fragments, we ended up four different configurations of dyclonine.

Preliminary analysis of dihedrals of χ_1 , χ_2 and χ_3 for 10 ns simulations are shown in Figure 2.5. C_1 , C_2 , C_3 and C_4 are shown with blue, green, cyan and red, respectively. For fragment 1, it is seen that dihedral χ_1 does not stick to initial angle and except $-50^\circ - 50^\circ$ interval, it can span all angles. Surprisingly, even though the energy barrier around -135° is high, dihedral can span this angle. On the contrary, dihedrals χ_2 and χ_3 of fragment 2 are not free to span all angles. While angle of χ_2 can reach -90° and 90° , χ_3 seem to be restricted within its initial dihedral angles.

2.1.2 Construction of Pure Lipid Bilayer

In order to build lipid bilayer, charmm-gui [20] was used. Dipalmitoylphosphatidylcholine (DPPC) was selected as model phospholipid which is widely used in molecular dynamics (MD) simulations. Model bilayer was composed of total 128 DPPC in which 64 of them were located at upper leaflet and 64 at the lower leaflet. The initial system

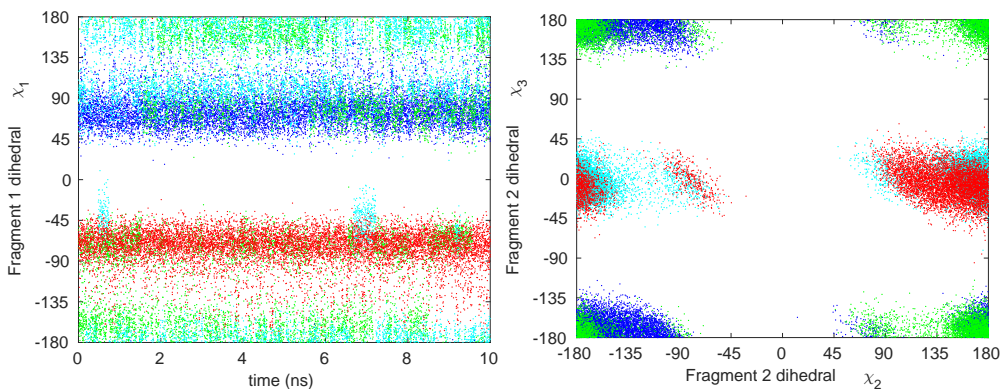


Figure 2.5: Dihedral χ_1 of fragment 1 is successful in spanning all the dihedral angles except $-50^\circ - 50^\circ$ interval where the energy barrier reaches 6 kcal/mol in 10 ns simulations (left). Dihedrals χ_2 and χ_3 are less capable of span larger intervals. While χ_2 can change up to -90° and 90° , χ_3 is restricted to initial values in 10 ns simulations.

included 7131 water molecules. Additionally 0.15 mM KCl ion was added which corresponded to 22 K^+ and 22 Cl^- ions. We used hexagonal simulation box with dimensions of approximately $6.8 \text{ nm} \times 6.8 \text{ nm} \times 9.5 \text{ nm}$.

First, the system was equilibrated with the methodology as it was recommended by charmm-gui. During this equilibration, lipids were slowly released from constraints for stability of the bilayer structure consistent with experimental studies. Constructed system was simulated for 13 ns. For all systems CHARMM36 force field was used with TIP3P water. Simulations were performed with NAMD [21]. Particle-mesh Ewald method was used to calculate electrostatic interactions, SHAKE algorithm was used to constrain the bond of hydrogen atoms. Pressure was set to 1 atm by Langevin piston and temperature was set to 323.15 K which is above of gel phase and provides perfect agreement between experimental and simulation studies for DPPC via Nose - Hoover thermostat [18]. Periodic boundaries were opened for continuity of the system.

2.2 Results

2.2.1 Charged Dyclonine

Modifications of system were performed on the last frame of 13 ns pure bilayer simulation. Eight charged dyclonine molecules were inserted into the aqueous environment of the simulation box in order to understand how they start to interact with the lipid bilayer. They were located at a distance of approximately 3 nm from the center of the bilayer (four of them were above and four of them below of the bilayer as shown in Figure 2.6). Two of each conformation of dyclonine were used. Water molecules overlapping with the inserted drug molecules were removed from the system. Four K^+ atoms were deleted and additional four Cl^- atoms were added in order to neutralize final system. Resulting sys-

tem included 128 DPPC, 18 K^+ , 26 Cl^- , 7003 water, and 8 drug molecules ($8D^+$ system). Simulation lasted for 250ns.

Initial and final configurations of the molecules are shown in Figure 2.6. In the illustration red, cyan, blue, brown, white colors represent oxygen, carbon, nitrogen, phosphorous and hydrogen atoms, respectively. Therefore small red dots indicate water molecules, cyan lines show carbon tails of lipid bilayer, brown balls show phosphorous atoms of lipid head, blue dots indicate nitrogen atoms of choline group of lipid head. It is seen that within 250 ns all eight dyclonine molecules have inserted themselves into the membrane.

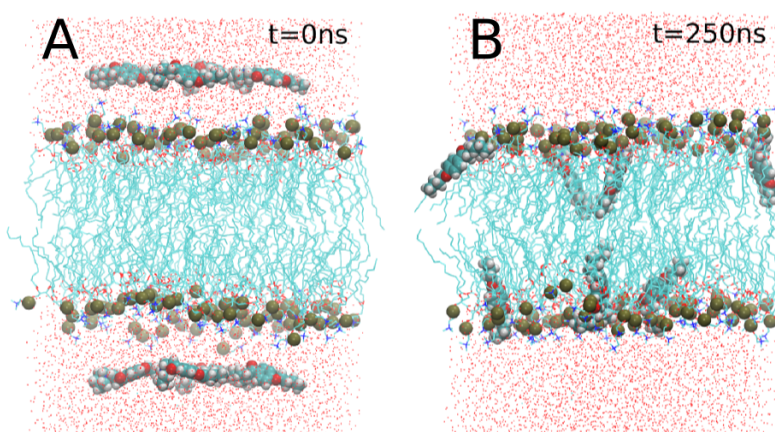


Figure 2.6: Eight charged dyclonine outside of the bilayer was simulated for 250 ns. All molecules are capable of penetrating into bilayer within simulation time. Red, cyan, blue, brown, white colors represent oxygen, carbon, nitrogen, phosphorous and hydrogen atoms, respectively.

In order to visualize charged dyclonine molecules' motion in the simulation box, time trace of eight molecules were drawn. Head groups of dyclonine molecules were selected to visualize their motion. We define membrane border with phosphorous atoms which are shown with brown and each configuration of dyclonine is shown with different color. In Figure 2.7A, we see that all penetration events are completed before 150 ns. In Figure 2.7B, position distributions of drugs, phosphorous atoms, lipid tail and water molecules are shown with black, brown, cyan and red, respectively. It is seen that dyclonine molecules locate at just below of phosphorous atoms in the bilayer. Additionally, drugs never change leaflet and they do not even enter into hydrophobic core of the membrane.

Inspection of the MD trajectories reveals that to enter into the bilayer the charged dyclonine molecules need to insert their tails first. One such insertion is shown in Figure 2.8 which is completed in 2 ns. Otherwise, when they approach to bilayer with their head groups they are unable to penetrate into bilayer. In Figure 2.7, one of the dyclonine molecules at upper leaflet, shown with red color around 50^{th} ns, approaches to the

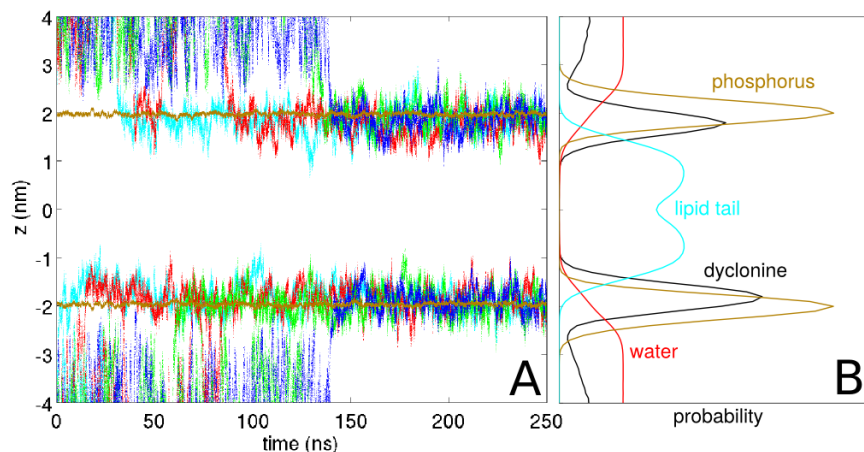


Figure 2.7: Time trace of eight charged dyclonine molecules (A) and their position distribution within the simulation box (B) are shown. Dyclonine molecules prefer to locate slightly below of the phosphorous atoms of the lipids.

bilayer with its head group (Figure 2.9). As it first introduces its head group into bilayer it is unable complete entrance into membrane. The molecule remains in this position for approximately 10 ns and then leaves the bilayer.

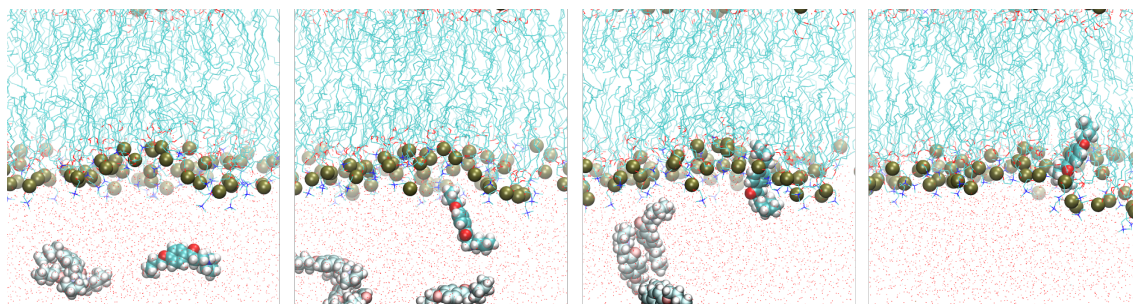


Figure 2.8: Dyclonine molecule should first introduce its tail into bilayer in order to complete insertion process. The insertion is completed in 2 ns. The color of interested dyclonine is shown opaque while other dyclonine molecules are shown metallic.

In addition, while dyclonine molecules move freely in aqueous environment, it is seen that when they penetrate into the bilayer they prefer to stay parallel to the bilayer normal. In order to determine their orientation quantitatively, we define a vector from tail (CG1, CK1, CK2 and CK3) to aliphatic ring (atoms of ND, CA, CB, CC, CD, CE and CM2) of the molecule and determine the angle of the vector with normal of the bilayer in positive direction ($+z$ direction) as it is shown in Figure 2.10. In Figure 2.11 orientation of eight dyclonines are shown separately. It is seen that four of the molecules stay around $z = 2$ nm with 0° indicating they reside their tails in $-z$ direction and similarly, other four molecules which stay around $z = -2$ nm orient their tails in $+z$ direction resulting the angle of 180° .

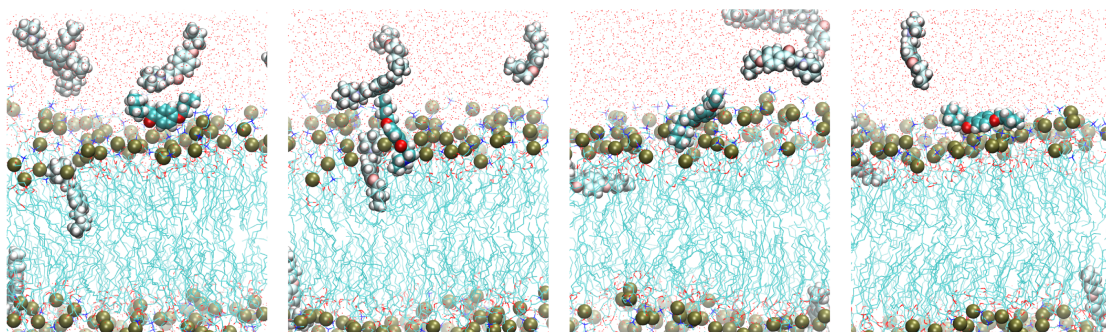


Figure 2.9: Dyclonine molecule fails to enter into bilayer since it first introduces its head group into bilayer. The shown process last approximately 10 ns. The color of interested dyclonine is shown opaque while other dyclonine molecules are shown metallic.

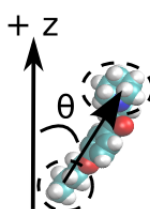


Figure 2.10: In order to determine the orientation of the molecules a vector is defined from tail (CG1, CK1, CK2 and CK3) to aliphatic ring of the molecule, and the angle of this vector with positive z direction is taken as θ .

2.2.2 Neutral Dyclonine

In addition to understanding the behavior of charged dyclonine, we aimed to figure out dyclonine behavior when it interacts with lipid bilayer in neutral state. Eight neutral dyclonine molecules were inserted into the system, again approximately 3 nm away from the bilayer center (Figure 2.12A) after 13 ns pure bilayer simulation. As before, each conformation of dyclonine was used twice. After inserting the molecules into the simulation box, overlapping water molecules were removed and resulting system included 128 DPPC, 22 K^+ , 22 Cl^- and 7006 water molecules ($8D^0$). System was simulated for 250 ns.

At $pH = 6.5$ (pH of yeast experiments), number of neutral dyclonine compared to charged dyclonine should be approximately 80 ($10^{(pK_a - pH)}$, $pK_a = 8.4$) times less than charged ones. Therefore, equal amount of charged and neutral dyclonine in aqueous environment is not experimentally realistic. However, as we can simulate any theoretical conditions with molecular dynamics simulations, we used the same amount of neutral dyclonine.

During 250 ns simulation, just one of the molecules was able to insert itself into the membrane (Figure 2.12B). Last snapshot of the simulation shows that other seven

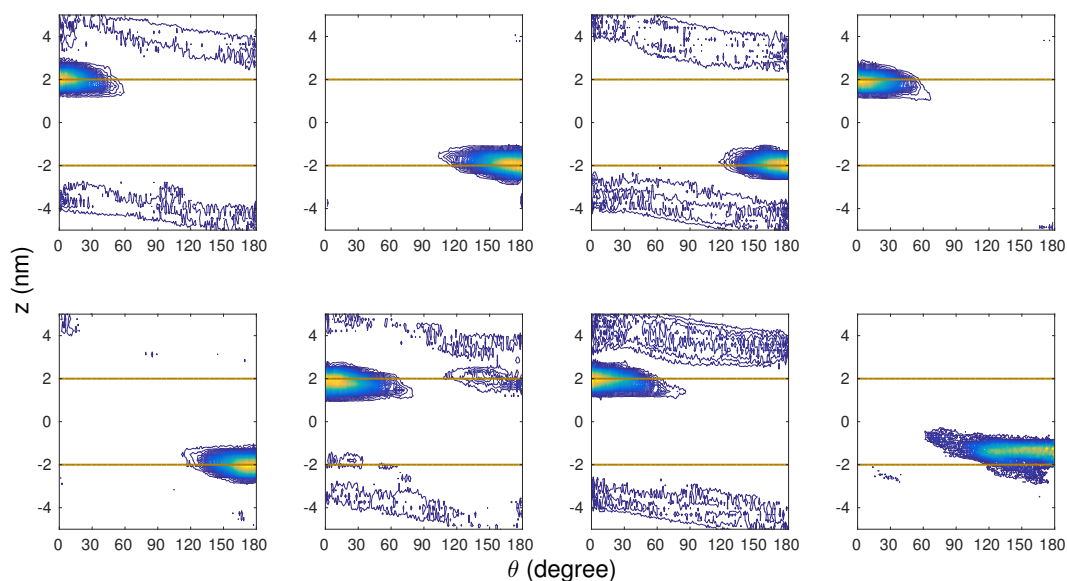


Figure 2.11: Charged dyclonine molecules stay parallel to normal of bilayer. The ones enter into the bilayer (bilayer borders are shown with brown lines) from upper leaflet stays with an angle 0° and the ones enter into bilayer from lower leaflet stays with an angle 180° . Cut-off selection for visualization allows to show orientation distribution of molecules in the water for just four dyclonine molecules while all molecules have the same distribution pattern in the water.

molecules stay together in water.

Time traces of neutral molecules were also analyzed. In Figure 2.13A, we see that only one of the dyclonine molecules enters into the bilayer while remaining ones stay in aqueous environment throughout 250 ns simulation. Position distributions are shown in Figure 2.13B. It is seen that the molecule which is capable of entering into lipid bilayer has changed lipid leaflet several times.

Similar with charged dyclonine, neutral one also insert its tail first (Figure 2.14). Since we have only one event for this process, it is difficult to generalize this behavior for all neutral dyclonine molecules.

When we analyze orientation of neutral dyclonine molecules we see that the ones stay at outside of the bilayer can be in any orientation, as expected (Figure 2.15). For the one which is capable of entering into lipid bilayer, we can indicate it slightly prefers to be parallel to lipid bilayer normal when it is closer to head groups and changes its orientation while changing leaflet.

As we can see from the last snapshot of the simulation system, neutral dyclonine molecules accumulate. In figure 2.16, we show the total (dashed line) number of charged (black) and neutral (red) dyclonine outside of the bilayer and the number of dyclonines that move as cluster (solid line). We see that neutral dyclonines come together before 10 ns and all float together till one of them enters into the bilayer around 40^{th} ns. After this time, the remaining seven molecules move as a cluster. Even though two of them

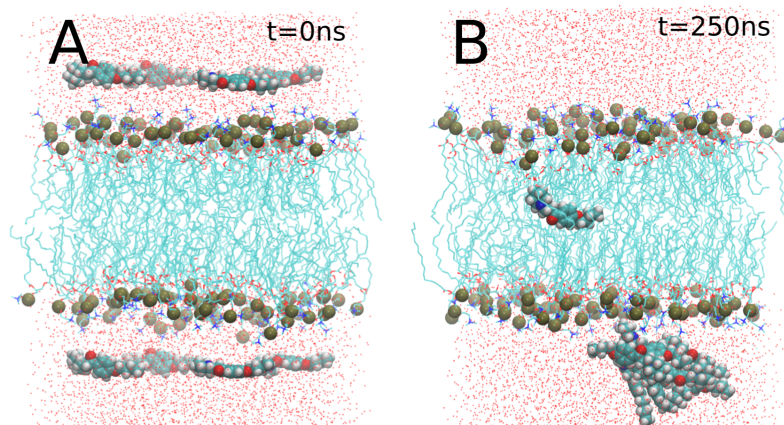


Figure 2.12: Eight neutral dyclonine outside of the bilayer was simulated for 250ns. Only one of them was successful in insertion process, remaining ones seem to be accumulated in water.

leave the aggregate twice, they reassemble within a few nanoseconds. When we look to behavior of charged dyclonine molecules we do not see a similar pattern. Although some of the charged ones come together, the number of accumulated molecules barely reach total number of molecules outside of the bilayer.

2.2.3 Neutral Dyclonine Inside the Bilayer

Since only one of the molecules in previous system was able to penetrate into lipid bilayer, four neutral dyclonine molecules were inserted into lipid bilayer in order to analyze their behavior inside of the model membrane.

In order to do that double lipid bilayer was constructed. For this purpose new bilayer was built via charmm-gui with 128 DPPC, 2560 water molecules and 0.15 mM KCl which corresponds to 4 K^+ and 4 Cl^- ions. The final system dimensions were 6.8 nm \times 6.8 nm \times 5.8 nm. Construction of double bilayer was completed via duplication and assembly of the newly generated membrane. Then, two dyclonine molecules were inserted into the center of each bilayer (4D⁰ system). For this system, each conformation of dyclonine was used once. System was simulated for 500 ns.

Initial and final configurations of the system are shown in Figure 2.17.

Position of each molecule with respect to time is shown in Figure 2.18. It is seen that all four dyclonine molecules move freely in z direction. Three of the molecules change the leaflet more than once during simulation, while the last one struggles with passing to the other leaflet. While this can be caused by structural difference, it may be just artifact of limited simulation time. Besides this bias of that dyclonine molecule (shown with red line), distribution of their localization shows there is slight preference to locations $|z| = 0, 1.1$ nm.

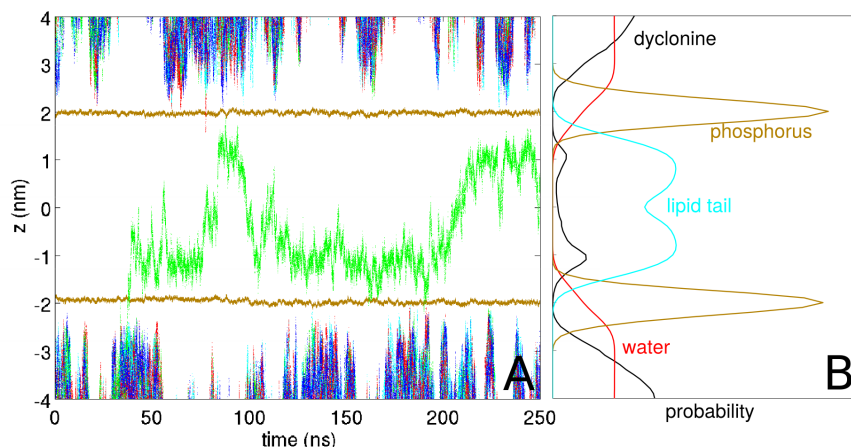


Figure 2.13: The one which is capable of enter into bilayer changes leaflet multiple times (A) and does not have a preferred location in simulation box along bilayer normal (B).

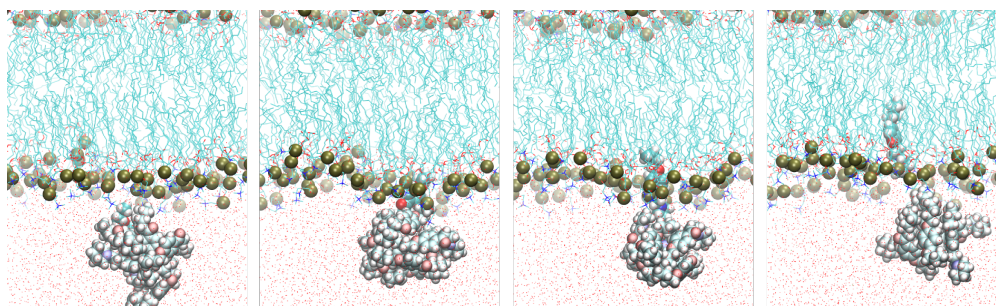


Figure 2.14: Similar with charged ones, neutral dyclonine also inserts its tail first into bilayer. The color of interested dyclonine is shown opaque while other dyclonine molecules are shown metallic.

Additionally, we aimed to understand whether molecules have specific orientations in the bilayer. It is seen that all four molecules prefer to stay parallel to bilayer normal at positions $z = 2$ nm and $z = -2$ nm as their head is close to head of phospholipids. Especially three of the molecules show very similar pattern that they prefer to stay parallel to bilayer normal around membrane borders and change their orientation while changing leaflet.

Figure 2.19 suggest molecules can change leaflet in two different paths. The average of four dyclonine molecules orientation distribution was averaged which is shown in Figure 2.20. Here, molecule may first change its orientation within the leaflet and then pass to the other leaflet (model I), or it may first change the leaflet and then arrange its orientation (model II).

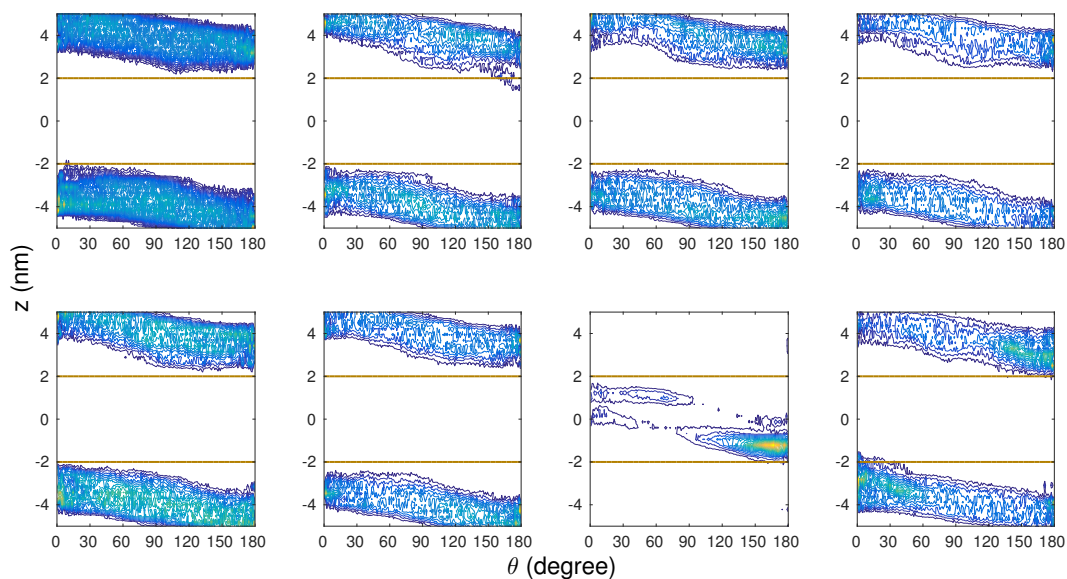


Figure 2.15: Neutral molecules which are unable to enter into bilayer (bilayer borders are shown with brown lines) can be in any orientation. The one which penetrates into bilayer changes its orientation with respect to the leaflet located in. At upper leaflet it stays with an angle of 0° , while at lower leaflet it stays with an angle of 180° .

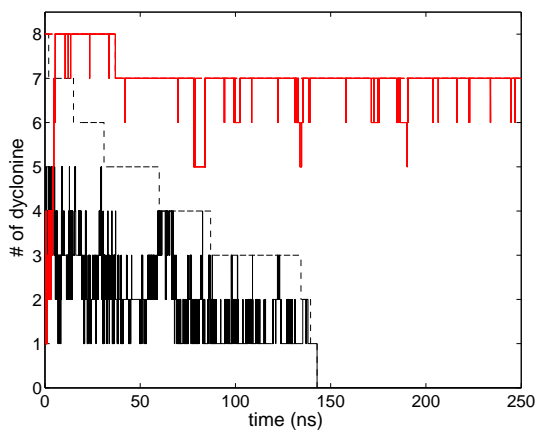


Figure 2.16: Accumulated (solid) and total (dashed) number of neutral (red) and charged (black) dyclonine molecules in aqueous environment are shown. It is seen that neutral dyclonine molecules form cluster within a few nanosecond and move as cluster for the rest of the simulation then while charged molecules do not accumulate.

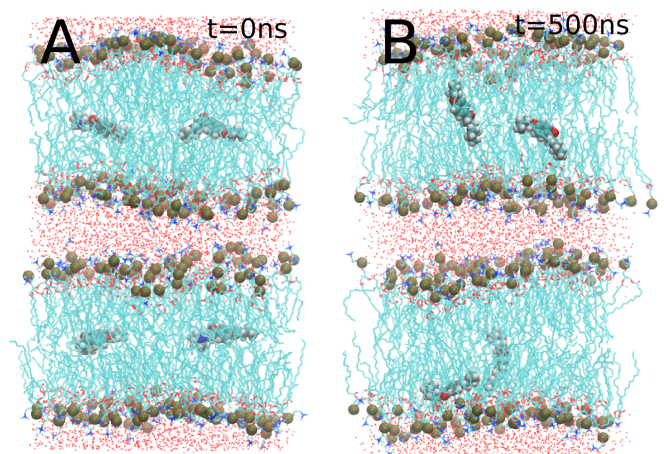


Figure 2.17: Behavior of neutral dyclonine molecules inside of the bilayer was studied by constructing double bilayer and introducing them to the center of the bilayer as initial condition.

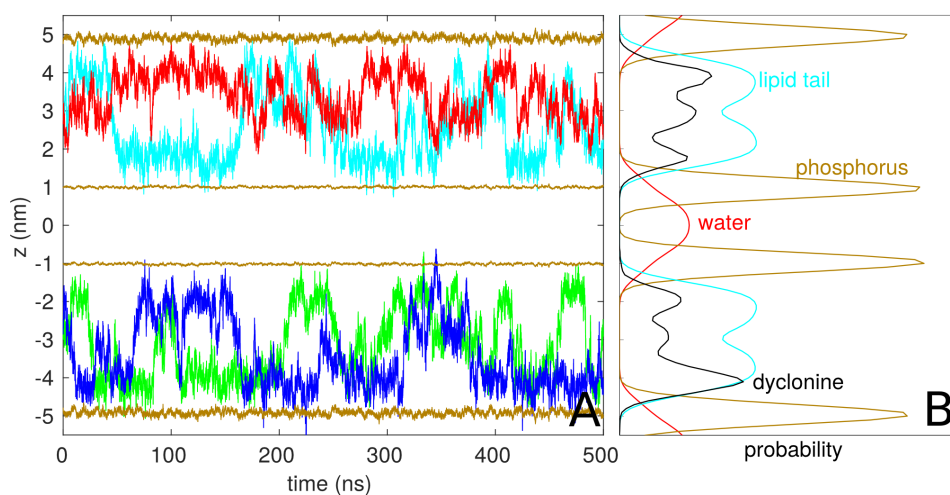


Figure 2.18: Neutral dyclonine molecules change leaflet multiple times during 500 ns simulations.

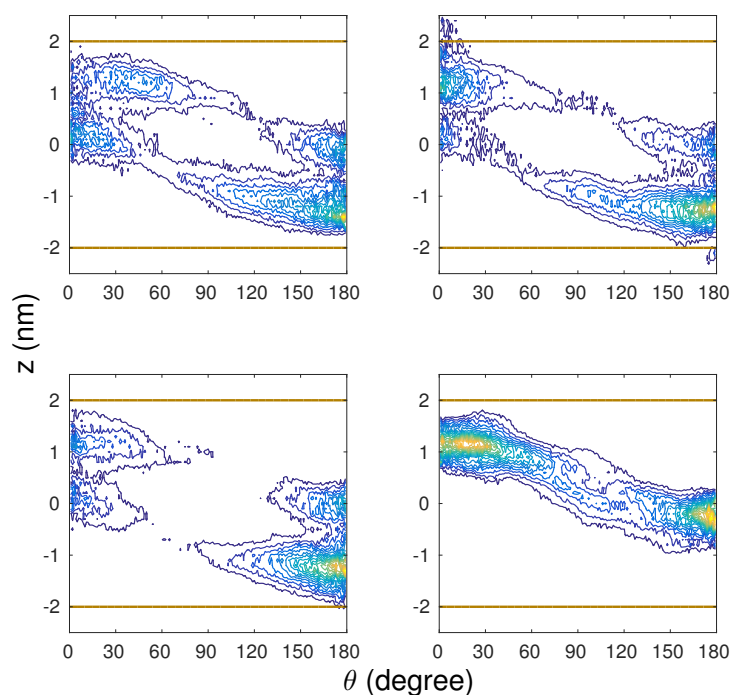


Figure 2.19: Distribution of angles of the defined vector (similar with $8D^+$) and $8D^0$ systems with respect to location along bilayer normal is shown. It is seen that while changing leaflet, they change their direction of orientation in one of the leaflets rather than changing it at the center of the bilayer. Membrane borders are shown with brown lines.

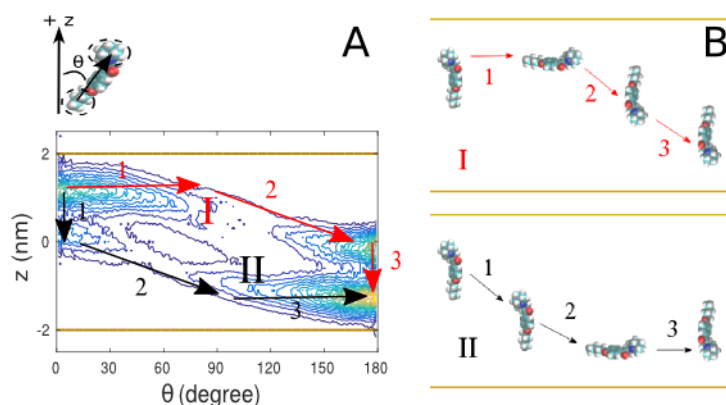


Figure 2.20: Tilt angle and averages of orientation distribution of four dyclonine molecules is shown (A). During translocation, drugs follow two paths. In model I, it changes its orientation within the leaflet it already located and then passes to the other leaflet. In model II, drug first crosses to the other leaflet and then changes its orientation (B).

2.3 Discussion

In order to understand the mechanism of drug permeation through lipid bilayer, MD simulations are widely used since it is possible to study drug - lipid interaction in atomistic details. MD simulations have been used extensively to study wide range of molecules including anticancer [22, 23], antiinflammatory [24, 25], antibacterial [26], anticonvulsant [27], local anesthetics [15] drugs and many small compounds [28, 29, 30, 31, 32, 33, 34] in lipid bilayer.

While it is possible to study only localization and orientation of drugs [26, 28, 35, 36] in the membrane, there are many other studies which also focus on their energy profile and permeability [27, 25, 33, 34]. These molecules include ionizable basic molecules like p-tyramine [33], arginine and lysine with their analogs [31], amitriptyline and clozapinetryptophan [37], tryptophan [34] in both charged and neutral states of the compounds. Local anesthetic drugs like benzocaine [13] and articaine [38] were also studied but only in their neutral states. Therefore, studying dyclonine with both states provides further insight about local anesthetic drug - lipid interaction and permeation.

MD simulations performed with dyclonine provides detailed information about behavior of both states of the drug interacting with lipid bilayer. It is seen that dyclonine molecules are able to enter into bilayer in both states. However we see that while neutral dyclonine is capable of changing leaflet, charged ones are stuck to the head groups of the phospholipids. Additionally, we do not see any dissociation events for both states within simulation times.

Position distribution of charged dyclonines clearly shows that they prefer to localize slightly below of the phosphorous atoms (Figure 2.7B). As dyclonines are positively charged and phosphate groups of lipids are negatively charged, it is expected to see this localization. Because of this electrostatic interactions charged dyclonines are unable to pass to other leaflet. On the other hand, neutral dyclonines inside of the bilayer are free to move along the bilayer normal within the membrane borders (Figure 2.13B, Figure 2.18B).

When we focus on how they insert into bilayer we see that both charged and neutral dyclonine molecules first insert their tail (Figure 2.8, Figure 2.14). Otherwise, if the molecule approaches to the bilayer with their head group, it is not possible for dyclonine to complete insertion process (Figure 2.9).

In the simulation system in which we initiated neutral dyclonines in aqueous environment, only one of them was able to enter into the bilayer. Normally, we expect that neutral dyclonine molecules should enter into lipid bilayer because dyclonine is a lipophilic molecule with logP 3.68. However we see that they aggregate in water in a very short time scale which prevents their penetration into lipid bilayer (Figure 2.16). This illustrates the importance of the solubility of the drugs. While we see this aggregation in neutral state,

we do not encounter such situation for charged molecules. As charged molecules are more soluble in water compared to neutral ones, they can move individually in the water which facilitates their permeation into bilayer.

As we analyze their orientation inside of the bilayer, we see that all charged molecules prefer to stay parallel to bilayer normal (Figure 2.11). Actually, with this orientation dyclonine molecules mimics phospholipids. Similar to phospholipids charged dyclonine has a hydrophilic and hydrophobic parts and they orient their hydrophobic part through bilayer core while keeping hydrophilic part around lipid heads.

For neutral dyclonine, it seems that when the molecule changes the lipid leaflet either it first changes its orientation direction (from being parallel in $+z$ direction to $-z$ direction, or vice versa) then passes to other leaflet, or it first passes to other leaflet and then changes its orientation direction (Figure 2.20). For the fourth molecule it is seen that it cannot pass to lower leaflet completely, it moves between $z = 2$ nm and $z = -0.5$ nm. At these edges it prefers to stay in parallel conformation to bilayer normal and can be in any orientation between these borders.

Overall, we can say that both charged states of dyclonine have different characteristics when they interact with the lipid bilayer. It is seen that neither of the states are capable of completing permeation process. While charged dyclonine can enter into bilayer it is unable to change its leaflet. On the other hand, neutral dyclonine can both penetrate into bilayer (even though we only have one event caused by accumulation in water) and passes to other leaflet.

Note that we do not see any dissociation events for both states. The reason why both charge states of the molecule can perform only specific parts of the permeation process is caused by heterogeneous structure of the lipid bilayer. Therefore analyzing the permeation of molecules in discrete states (insertion, translocation and dissociation) with three-layer perspective should provide deeper insight about overall process.

Chapter 3

Permeability from MD simulations

3.1 Theory and Methods

3.1.1 Diffusion Equation and Permeability

Drugs permeate through lipid bilayer into the cell (or liposome) as long as outside concentration is greater than the inside concentration. This concentration difference induces molecules to flow through the lipid bilayer. Therefore, flux density of drugs is proportional to the concentration difference which is described as,

$$j = \mathcal{P} \Delta c, \quad (3.1)$$

where $\Delta c = c_{out} - c_{in}$. Here, this proportionality constant is the permeability coefficient.

Permeability coefficient of a molecule is an indicator of how fast that molecule can pass through the membrane. In other words, it is the "conductivity" of the membrane for this specific molecule.

As the molecule diffuses along the bilayer normal, the change of concentration follows the Smoluchowski equation,

$$\frac{\partial c}{\partial t} = -\frac{\partial j}{\partial z} = -\frac{\partial}{\partial z} \left[-D(z) \frac{\partial c}{\partial z} + D(z) f(z) c \right], \quad (3.2)$$

where $c(z, t)$ is the drug concentration, $j(z, t)$ is the current density, $D(z)$ is the diffusion coefficient, and $f(z) = -u'(z)$ is the force where $u(z) \equiv G(z)/RT$ ($G(z)$ is the free energy along z , R is the gas constant, and T is the absolute temperature.)

Smoluchowski equation, (3.2), leads to determine permeability coefficient of molecules via the relation (3.3) which was originally proposed by Marrink and Berendsen [39]

$$\frac{1}{\mathcal{P}} = \int_{-L}^L dx \frac{e^{\Delta u(x)}}{D(x)} \quad (3.3)$$

where $\Delta u(x)$ is the energy difference of the molecule being at position x and being in

aqueous environment ($\Delta u(x) = u(x) - u_{out}$) and $D(x)$ is diffusion coefficient at corresponding position. Lets assume $-L$ corresponds to a point outside of the cell and L corresponds a point inside of the cell since the drug is applied from outside of the cell. Note that due to the symmetry of the membrane $\Delta u(x) = \Delta u(-x)$ and $D(x) = D(-x)$ where center of membrane is fixed to $x = 0$ nm.

It is seen that in order to estimate permeability coefficient of dyclonine, we need to have free energy and diffusion profiles along lipid bilayer.

3.1.2 Free Energy Profiles from Umbrella Sampling Simulations

In order to be able to determine complete profile of free energy of charged and neutral dyclonine, umbrella sampling (US) [40] methodology was used. With this method, system of interest is simulated individually with introducing artificial potentials to specific "windows" along reaction coordinate. For our system, as we want to obtain the energy profile between two states which are the situations that the molecule is in the aqueous environment ($z = 4$ nm) and at the center of the bilayer ($z = 0$ nm), the reaction coordinate of our system is simply $z = 4$ nm - $z = 0$ nm. For US simulations, separate umbrellas were generated with certain distances between two windows.

Construction of the complete profile was performed by combining the information from all these individual simulations. Weighted Histogram Analysis Method (WHAM) can be used to combine all these information from different simulations with biased potential [41]. This method aims to merge the data from all simulations on the basis of maximum overlapping method [42]. While the method developed by Bennet which combines the information of neighboring windows that have the highest overlap, WHAM provides combination of all umbrellas resulting unbiased profile with minimum statistical error.

For umbrella sampling simulations, center of mass of the head groups of dyclonine molecules were restrained to specific locations (windows) along the lipid bilayer normal. For a specific restraining position, same simulation box was used for the two states of the molecule. For example, for the umbrella of $z = 4$ nm charged dyclonine was restrained to $z = +4$ nm while neutral dyclonine was restrained to $z = -4$ nm. As example, initial views are shown in Figure 3.1 for umbrellas $|z| = 4$ nm, $|z| = 2.1$ and $|z| = 1.1$ nm. Since our simulation box is greater than 9 nm, two molecules did not interact with each other even at $z = 4$ nm through periodic boundaries.

On the other hand, to eliminate the interaction while restraining positions get closer to each other inside of the membrane, separate simulation boxes were used for the umbrellas smaller than $z = 1.1$ nm. In Figure 3.2 the initial view of the system where $|z| = 0.6$ nm is shown.

Selected positions along lipid bilayer, corresponding force constants and simulation durations are given in Table 3.1. For the positions 3 nm $\leq |z| \leq 4$ nm along reaction

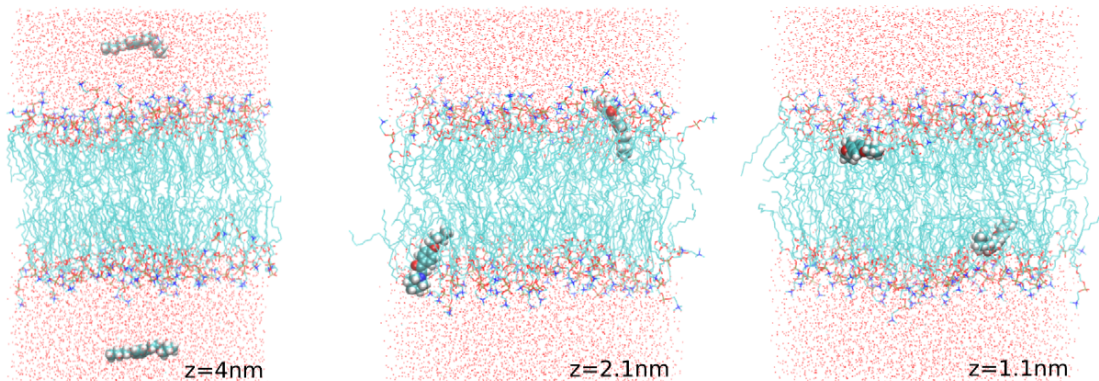


Figure 3.1: Both charged (up) and neutral dyclonine (down) molecules were inserted into the same system which provided time efficiency. Initial views of the simulation boxes are shown for $|z| = 4, 2.1$ and 1.1 nm windows.

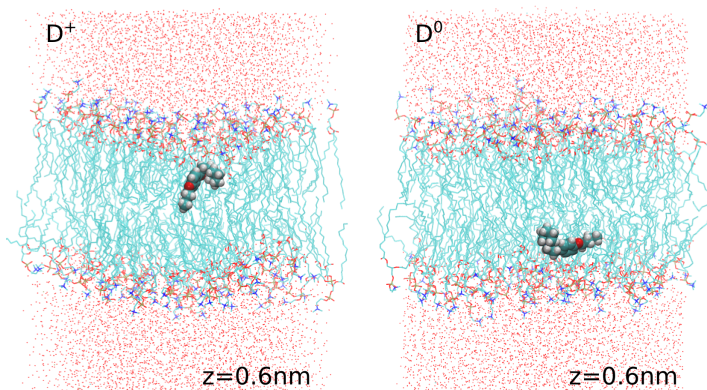


Figure 3.2: Simulations systems of charged (left) and neutral (right) were separated for the umbrellas $|z| \leq 1$ nm in order to eliminate the interaction of two dyclonine molecules.

coordinate umbrellas were placed with 0.5 nm distances. In order to obtain overlapped position distributions of two neighbor umbrellas, spring constants for these umbrellas were selected relatively small ($f = 0.5 \text{ kcal mol}^{-1} \text{ \AA}^{-2}$, $f = 0.15 \text{ kcal mol}^{-1} \text{ \AA}^{-2}$ and $f = 0.5 \text{ kcal mol}^{-1} \text{ \AA}^{-2}$ for $|z| = 4$ nm, $|z| = 3.5$ nm and $|z| = 3$ nm, respectively). The interval between two neighboring umbrellas were decreased up to 0.1 nm as the drugs approached to lipid bilayer. Therefore spring constants were increased and kept at $2 \text{ kcal mol}^{-1} \text{ \AA}^{-2}$ for the umbrellas $|z| < 2.6$ nm. As it was mentioned before, separate simulation boxes were used for the positions $|z| < 1.1$ nm. For neutral dyclonine interval of the umbrellas was increased to 0.2 nm and spring constants were decreased to $1 \text{ kcal mol}^{-1} \text{ \AA}^{-2}$ and $0.8 \text{ kcal mol}^{-1} \text{ \AA}^{-2}$.

In order to obtain unbiased profile, position distributions of each window should overlap with at least its closest neighbors. To check it, position distributions of both charged (Figure 3.3, left) and neutral (Figure 3.3, right) molecules were plotted. It is seen that each umbrella overlaps at least with its closest neighbors' distributions.

z/nm	$k/\text{kcal mol}^{-1}\text{\AA}^{-2}$		T/ns	
	D^+	D^0	D^+	D^0
4.0		0.5		20
3.5		0.15		20
3.0		0.5		15
2.8		0.8		15
2.6		1.0		15
2.5-2.1		2.0		15
2.0		2.0		20
1.9-1.4		2.0		15
1.3		2.0		20
1.2-1.1		2.0		15
1.0	2.0	1.0		15
0.9	2.0	-	15	-
0.8	2.0	0.8	15	20
0.7	2.0	-	15	-
0.6	2.0	0.8	15	20
0.5	2.0	-	15	-
0.4	2.0	0.8	15	20
0.3	2.0	-	15	-
0.2	2.0	0.8	15	20
0.1	2.0	-	15	-
0	2.0	0.8		15

Table 3.1: Harmonic force constants (k) and total simulation time (T) for corresponding restraining positions (z) of the umbrella potentials.

3.1.3 Local Estimate of Diffusion

Diffusion coefficients can be determined locally from position time correlation functions (pTCF). Hummer [43] states that

$$D(Z) = \frac{[\text{Var}(z_Z)]^2}{\int_0^\infty dt \langle \delta z_Z(\tau + t) \delta z_Z(\tau) \rangle_\tau}, \quad (3.4)$$

where z_Z is the position of the molecule restrained at location Z , $\bar{z}_Z = \langle z_Z(t) \rangle_t$ is the average of the position for that specific umbrella at Z and $\delta z_Z(t) = z_Z(t) - \bar{z}_Z$ denotes the deviation of z_Z from its average.

Note that the denominator in (3.4) is the area under the pTCF,

$$C_Z(t) = \langle \delta z_Z(\tau + t) \delta z_Z(\tau) \rangle_\tau, \quad (3.5)$$

In order to estimate (3.5), we fit each umbrella's pTCF to exponentially decaying functions. While correlation functions perfectly fit to monoexponential function in aqueous environment, it is hard to postulate it for the umbrellas smaller than $|z| = 3.0\text{nm}$. Therefore curves below of that point are needed to fit to di- and even tri- exponential functions.

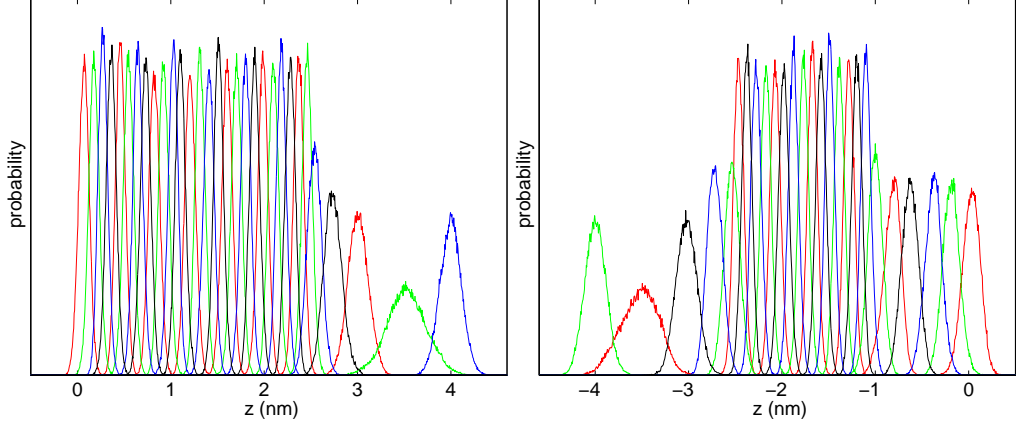


Figure 3.3: Position distributions of both charged (left) and neutral (right) dyclonine molecules are successful in overlapping with their neighbors' distributions.

$$C_Z(t) = \sum_{n=1}^m a_{Z_n} e^{-t/\tau_{Z_n}}, \quad (3.6)$$

where m equals to 1, 2 or 3 for mono-, bi- or tri- exponential functions, respectively.

All umbrellas along reaction coordinate were fit to mono-, bi- and tri- exponential functions to see the difference better. As it is seen in Fig. 3.4, there is no notable difference in mono-, bi- and tri- exponential fits for both D^+ and D^0 at $z = 4.0$ nm where the molecules locate in water. On the other hand, as it is seen in Fig. 3.5 while mono- and bi-exponential functions are unsuccessful to fit to data at the center of the membrane ($z = 0$ nm), tri- exponential function fits better to pTCF of D^0 (right) and almost perfectly to pTCF of D^+ (left). Note that in order to correct the difference in scale of pTCF caused by usage of different spring constants for umbrellas, both x and y axes are multiplied with f/RT of that umbrella where f is spring constant, R is gas constant and T is temperature (see Table 3.1 for force constants).

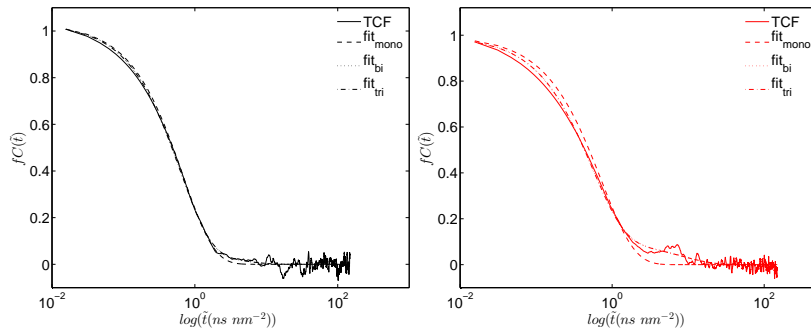


Figure 3.4: pTCFs (solid) in aqueous environment ($z = 4$ nm) are fit to mono- (dashed), bi- (dotted) and tri- (dotted dash) exponential functions for charged (black, left) and neutral (red, right) dyclonine molecules. Both axes are rescaled with corresponding force constants, f/RT .

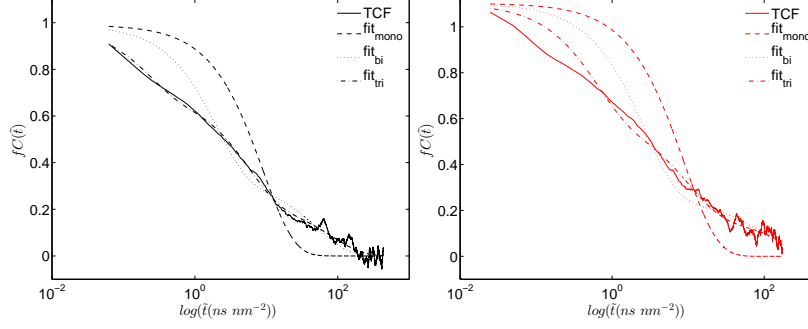


Figure 3.5: pTCFs (solid) at the center of bilayer ($z = 0$ nm) are fit to mono- (dashed), bi- (dotted) and tri- (dotted dash) exponential functions for charged (black, left) and neutral (red, right) dyclonine molecules. Both axes are rescaled with corresponding force constants, f/RT .

Fitting the pTCFs to bi- and tri- exponential functions reveals that there are motions with different time scales. The need to fit the pTCFs to more than one exponential does not occur when the molecule was in the aqueous environment as mentioned before. Since it arises when the molecule starts to approach to the bilayer the reason can be the interaction of molecule with lipids.

While fitting pTCF, it was noticed that for some umbrellas τ_Z coefficient of slowest component was unrealistically high since correlation functions do not converge to zero. Therefore these coefficients were restricted with boundaries.

In order to determine the “goodness” of the fits of all three exponentials quantitatively, difference between pTCF and fit functions was defined as error. Error was calculated as,

$$E(z) = \int_{t_i}^{t_f} |C_C(\tilde{t}) - C_F(\tilde{t})| d\tilde{t}, \quad (3.7)$$

where $C_C(\tilde{t})$ is the calculated value and $C_F(\tilde{t})$ is the fit value for corresponding time point in the correlation functions. $t_i = 0$ ns and $t_f = 1.4$ ns $\times f/k_B T$. Estimation of the error was done for the logarithmic scale of the time axis in order to increase the participation of the points in the fast decaying part of the correlation function.

Calculated errors for both D^+ and D^0 are shown in Fig. 3.6. It is seen that while errors of monoexponential functions are fairly low in aqueous environment, for the umbrellas $z \leq 2.8$ nm errors are pretty high for dyclonine. Additionally, it is seen that both bi- and tri- exponential functions fit better than monoexponential functions throughout the reaction coordinate. Also, triexponential functions are better than biexponential functions.

Diffusion coefficients for all mono-, bi- and tri- exponential functions are calculated for both charged (black) and neutral (red) states (Fig. 3.7). It is seen that diffusion coefficients calculated from monoexponential fits are apparently different from the ones calculated from bi- and tri- exponentials. On the other hand, diffusion coefficients estimated from bi- and tri- exponential fits are not much different from each other yet they are same

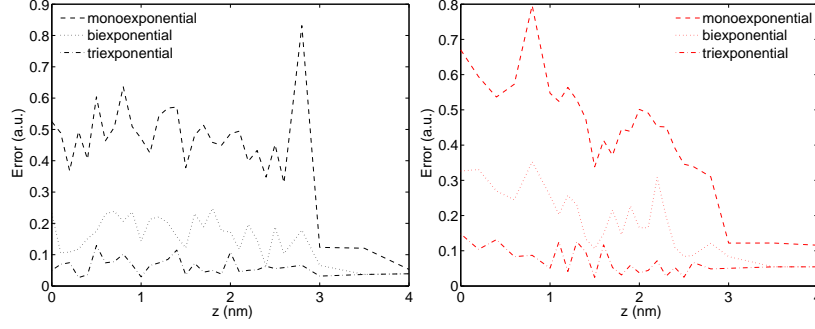


Figure 3.6: Errors of mono- (dashed), bi- (dotted) and tri- (dotted dashed) exponential functions for charged (black, left) and neutral (red, right) dyclonine are shown.

for most of the points even though the success of fits (errors) are different. Therefore, for the umbrellas in the water ($z = 3, 3.5$ and 4 nm) diffusion coefficients of monoexponential functions, for the rest of the umbrellas diffusion coefficients of biexponentials are used for local estimate of diffusion.

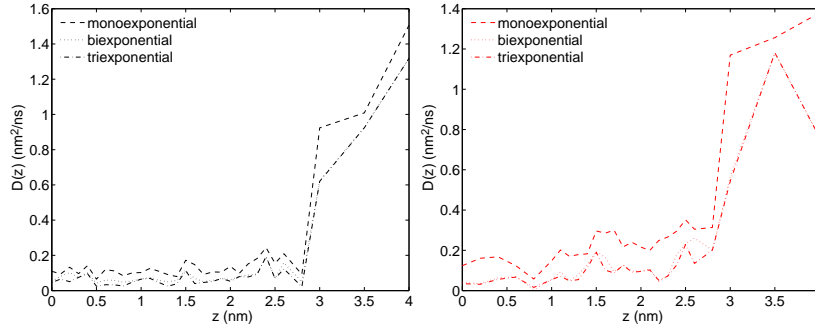


Figure 3.7: Diffusion coefficients calculated from mono- (dashed), bi- (dotted) and tri- (dotted dashed) exponential functions for charged (black, left) and neutral (red, right) dyclonine are shown.

3.1.4 Global Estimate of Diffusion Profile

Various mean first passage times for 1D diffusion in a potential are available. For $a < z < x$ with a reflecting boundary at a and an absorbing boundary at x the MFPT is[44]

$$\tau_{\rightarrow x}^{|ax\rangle}(z) = \int_z^x d\zeta \frac{e^{u(\zeta)}}{D(\zeta)} \int_a^\zeta d\eta e^{-u(\eta)}. \quad (3.8)$$

Note that, because this expression contains the product of $e^{u(\zeta)}$ and $e^{-u(\eta)}$, the arbitrary zero reference of the free energy $u(z)$ is immaterial, as long as the same reference point is used consistently. Similarly, for $x < z < b$ with an absorbing boundary at x and a

reflecting boundary at b the MFPT is[44]

$$\tau_{x \leftarrow}^{<xb|}(z) = \int_x^z d\zeta \frac{e^{u(\zeta)}}{D(\zeta)} \int_\zeta^b d\eta e^{-u(\eta)}. \quad (3.9)$$

Netz and coworkers have introduced the round-trip (τ_{rt}) time, which is the MFPT to go from z to x plus the MFPT to go from x to z . For $a < x < z < b$, with reflecting boundaries at a and b the τ_{rt} is

$$\tau_{x \rightleftharpoons}^{|ab|}(z) = \tau_{x \leftarrow}^{<xb|}(z) + \tau_{\rightarrow z}^{|az>}(x) = Z_{ab} \int_x^z d\zeta \frac{e^{u(\zeta)}}{D(\zeta)}, \quad (3.10)$$

where

$$Z_{ab} = \int_a^b d\eta e^{-u(\eta)}. \quad (3.11)$$

For the diffusion profile this leads to

$$D_{x \rightleftharpoons}(z) = \frac{Z_{ab} e^{u(z)}}{d\tau_{x \rightleftharpoons}^{|ab|}(z)/dz}. \quad (3.12)$$

Similarly, when z is between a and x ($a < z < x < b$), the τ_{rt} is

$$\tau_{\rightleftharpoons x}^{|ab|}(z) = \tau_{\rightarrow x}^{|ax>}(z) + \tau_{z \leftarrow}^{<zb|}(x) = Z_{ab} \int_z^x d\zeta \frac{e^{u(\zeta)}}{D(\zeta)}, \quad (3.13)$$

and the resulting diffusion profile is

$$D_{\rightleftharpoons x}(z) = -\frac{Z_{ab} e^{u(z)}}{d\tau_{\rightleftharpoons x}^{|ab|}(z)/dz}. \quad (3.14)$$

In our analysis, we use the drug trajectories in the free (unrestrained) MD simulations to obtain estimates of the τ_{rt} , $\tau_{x \rightleftharpoons}^{|ab|}(z)$ and $\tau_{\rightleftharpoons x}^{|ab|}(z)$ for several values of $z \in (a, b)$. When estimating $\tau_{x \rightleftharpoons}^{|ab|}(z)$ we choose $x = a$, whereas for $\tau_{\rightleftharpoons x}^{|ab|}(z)$ we choose $x = b$. We denote the diffusion profiles obtained from these τ_{rt} by $D_{a \leftarrow}$ and $D_{\rightarrow b}$, respectively.

Since both D^+ and D^0 do not show a complete process of permeation in free simulations, we determined to introduce virtual boundaries along bilayer which provide estimation of the diffusion profiles as fragments. Reaction coordinate was divided into four regions given in Table 3.2 and Figure 3.8.

Round trip time (RTT) values along bilayer normal were determined with 0.05 nm resolution. As explained above, RTT is the summation of two mean first passage times (MFPTs) which are (i) time for a molecule starting from an initial point within the interval (restricted with one absorbing and one reflecting boundaries) till arriving to its absorbing boundary and (ii) time for that molecule restarting from the absorbing boundary till reaching back the initial point. In order to estimate RTTs, averages of $T_{x \leftarrow}^{<xb|}(z)$ and $T_{\rightarrow z}^{|az>}(x)$ (or

regions	range
I	-1.4 nm - 1.4 nm
II	1.4 nm - 2.6 nm
III	2.6 nm - 3.0 nm
IV	3.0 nm - 4.0 nm

Table 3.2: Fragments of reaction coordinate separated by virtual boundaries for estimation of τ_{rt} .

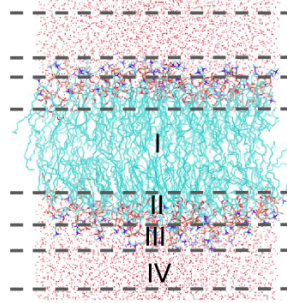


Figure 3.8: Reaction coordinate was divided into four regions with virtual boundaries.

$T_{\rightarrow x}^{|ax>}(z)$ and $T_{z\leftarrow}^{|zb|}(x)$ are summed. Observed events were divided into three groups, and each of them had approximately equal number of events. Standard deviation of $T_{x\rightleftharpoons}^{|ab|}(z)$ (or $T_{\rightleftharpoons x}^{|ab|}(z)$) was determined by the relation $\sigma_{rt} = \sqrt{\sigma_{x\leftarrow}(z)^2 + \sigma_{\rightarrow z}(x)^2}$.

For diffusion profile of dyclonine in region I, 480 ns $4D^0$ and 250 ns $8D^0$ simulations were used. For determination of $T_{x\rightleftharpoons}^{|ab|}(z)$, first $\tau_{x\leftarrow}^{|zb|}(z)$ and $T_{\rightarrow z}^{|ax>}(x)$ should be calculated. In Figure 3.9 left panel, time is given for a molecule starting from an initial point within the interval and reaching absorbing boundary and at right panel time is given for the molecule restarting from absorbing boundary and reaching back the initial point. In both graphs we see monotonically increasing plots as expected since time increases as the distance between absorbing boundary and initial point expands.

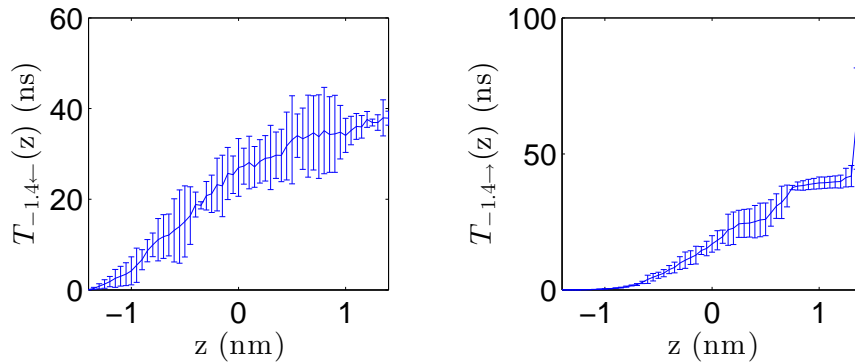


Figure 3.9: $T_{x\leftarrow}^{|zb|}(z)$ and $T_{\rightarrow z}^{|ax>}(x)$ values which are calculated from $8D^0$ simulations for region I

In the $T_{\rightarrow z}(x)$ plot, there is a jump between $z = 1.3$ nm and $z = 1.4$ nm. The reason is there are some events in which the molecules can reach to $z = 1.3$ nm and turns back without touching $z = 1.4$ nm (and touches to $z = 1.4$ nm later, data not shown) which automatically increases the duration. Since our sampling is limited, these kind of artifacts are inevitable.

Summation of $T_{x\leftarrow}(z)$ and $T_{\rightarrow z}(x)$ for each point gives the round-trip time (Figure 3.10, left panel). Even though overall graph shows a monotonically increasing pattern, we see there are points that is lower than the previous ones which leads a negative slope resulting negative diffusion coefficient. In order to avoid this unrealistic diffusion profile, $T_{x\rightleftharpoons}^{|ab|}(z)$ is smoothed with using five (blue) and seven (black) points. Calculated diffusion values are shown in Figure 3.10 right panel. Although smoothing works for most of the points, it is inevitable to see jumps where the slope of $T_{x\rightleftharpoons}^{|ab|}(z)$ is small. This problem is partially overcome by increasing the number points used for smoothing. We see that even though smoothing with different numbers of points do not affect the $T_{x\rightleftharpoons}^{|ab|}(z)$ profile, it leads more apparent difference in diffusion profile. Furthermore, there is an increase at absorbing boundary which is not unique to this interval.

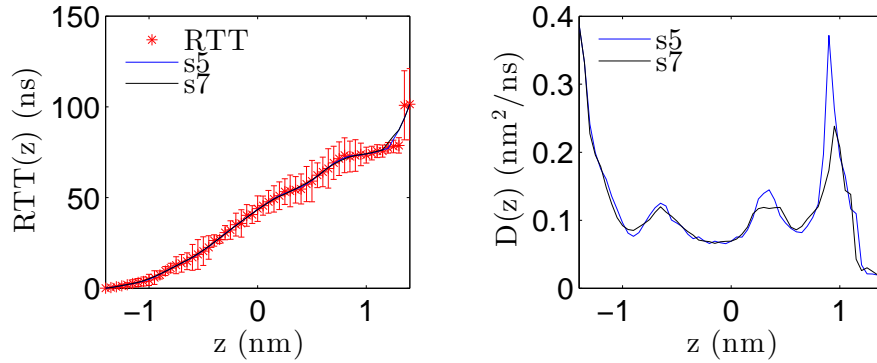


Figure 3.10: $T_{x\rightleftharpoons}^{|ab|}(z)$ profile was determined from free simulations (left). Red stars show MD data, blue and black lines show smoothed values with five and seven points, respectively. Diffusion profiles were determined from smoothed $T_{x\rightleftharpoons}^{|ab|}(z)$ values (right).

$T_{\rightarrow x}^{|ax>}(z)$ and $T_{z\leftarrow}^{|zb|}(x)$ values for the same interval shown in Figure 3.11. Again in the left panel, time is shown for each initial point within the interval till reaching to absorbing boundary ($z = 1.4$ nm) ($T_{\rightarrow x}^{|ax>}(z)$). In the right panel duration is shown starting from the absorbing boundary to arriving initial point ($T_{z\leftarrow}^{|zb|}(x)$). Both plots are decreasing monotonically as expected since the starting point getting closer to absorbing boundary except the first two points of figure on the right. The reason is there are two events in which crossing starts from absorbing boundary and reaches to $z = 1.3$ nm in a long duration which never touches to $z = 1.4$ nm so this long duration is counted for $z = 1.3$ nm but not $z = 1.4$ nm (data not shown).

$T_{\rightleftharpoons x}^{|ab|}(z)$ is shown in Figure 3.12, left panel. Data was smoothed for five and seven points again. Diffusion profiles were obtained for these two curves of RTTs (Figure 3.12,

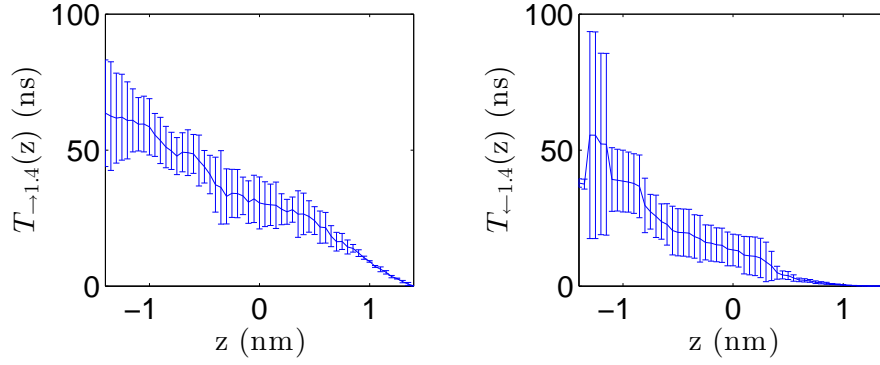


Figure 3.11: $T_{\rightarrow x}^{|ax\rangle}(z)$ and $T_{z\leftarrow}^{\langle zbl\rangle}(x)$ values which are calculated from $8D^0$ simulations for region I

right panel). We see that diffusion profiles give unrealistic diffusion values at reflecting boundary because of positive slope which results negative diffusion values. Moreover, there is an increase at absorbing boundary.

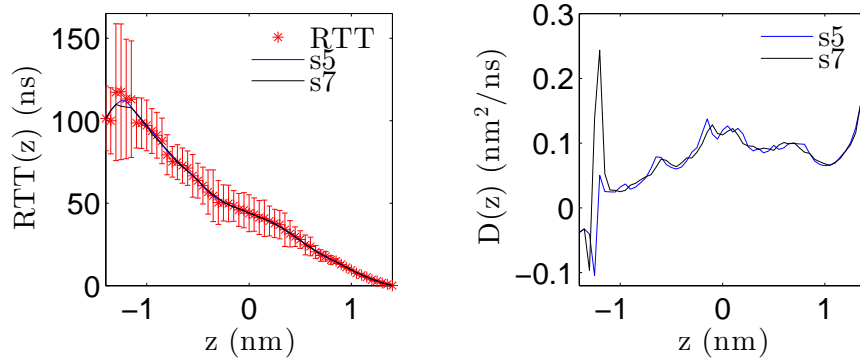


Figure 3.12: $T_{\rightleftharpoons x}^{|abl\rangle}(z)$ determined from free simulations (left). Red stars show data, blue and black lines show smoothed data with five and seven points, respectively. Diffusion profiles determined with smoothed RTT values (right).

Profiles of $T_{x\rightleftharpoons}^{|abl\rangle}(z)$ and $T_{\rightleftharpoons x}^{\langle abl\rangle}(z)$ directions for $z = -1.4$ nm and $z = 1.4$ nm interval is shown in Figure 3.13. Same analysis performed for the interval of $z = -1.0$ nm and $z = 1.0$ nm to see whether we can obtain similar profiles, in other words, whether choice of virtual borders effect the resulting profile or not. It is seen that obtained profiles are consistent with each other suggesting boundary selection does not effect the diffusion profile. Additionally, we still see increased diffusion values closer to absorbing boundary. Actually, these jumps at absorbing boundary is also shown in other studies which use MFPT to determine diffusion coefficients [45]. The reason is explained as the non-Markovian motion of the molecule at smaller time scales which arises at absorbing boundary.

Using similar strategies diffusion coefficients of $z = 1.4$ nm and $z = 2.6$ nm interval were determined. For determination of τ_{rt} for this interval $8D^+$ free simulations were used. RTT data points are again smoothed with five and seven points. It is seen that

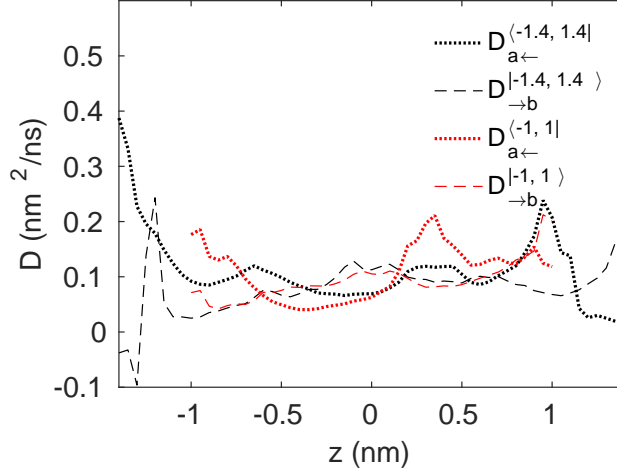


Figure 3.13: Diffusion profiles are shown for $z = -1.4 \text{ nm} - z = 1.4 \text{ nm}$ (black) and $z = -1.0 \text{ nm} - z = 1.0 \text{ nm}$ (red) intervals.

for both $T_{x\leftarrow}^{|ab|}(z)$ (Figure 3.14) and $T_{\rightarrow x}^{|ab|}(z)$ (Figure 3.15), there is not much difference between two smoothing strategies in both RTT and diffusion profiles. Not surprisingly, in both directions there is an increasing profile at absorbing boundary as $z = -1.4 \text{ nm} - z = 1.4 \text{ nm}$ interval.

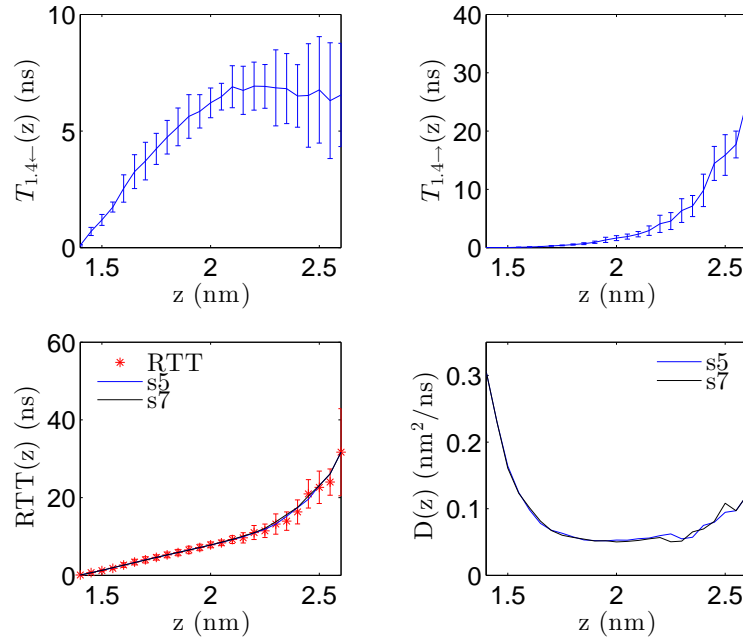


Figure 3.14: $T_{x\leftarrow}^{\langle ab|}(z)$, $\tau_{\rightarrow z}^{\langle az \rangle}(x)$, $\tau_{x\rightarrow}^{\langle ab|}(z)$ and diffusion profiles for region II.

We cannot determine diffusion profile for region III since we do not have enough sampling to determine RTT in this interval. For the estimation of RTT we need to have events in which molecules move through both directions along bilayer normal. However as we do not see any dissociation event in our $8D^+$ simulation system, there is no molecule moving in both directions within this interval.

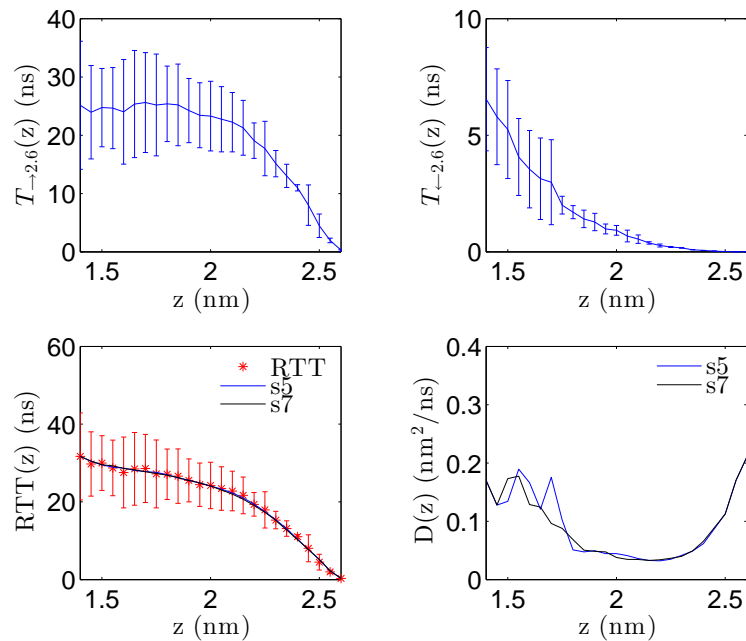


Figure 3.15: $T_{\rightarrow x}^{|ax\rangle}(z)$, $\tau_{z\leftarrow}^{\langle zb\rangle}(x)$, $T_{\rightleftharpoons x}^{|ab\rangle}(z)$ and diffusion profiles for region II.

Lastly, region IV was analyzed for both $T_{x\leftarrow}^{|ab\rangle}(z)$ (Figure 3.16) and $T_{\rightleftharpoons x}^{|ab\rangle}(z)$ (Figure 3.17) to determine diffusion profile in aqueous environment.

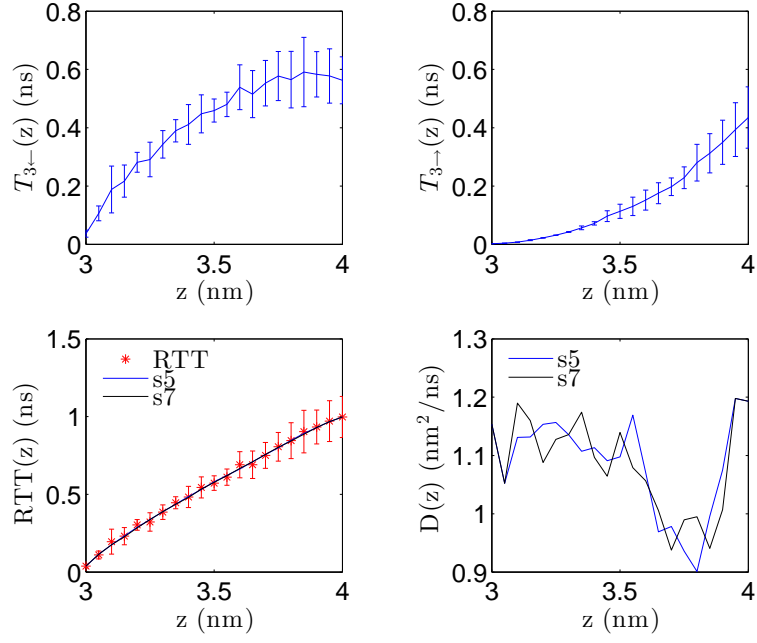


Figure 3.16: $T_{x\leftarrow}^{<xb|}(z)$, $T_{\rightarrow z}^{|az>}(x)$, $T_{x\rightleftarrows}^{|ab|}(z)$ and diffusion profiles for region IV.

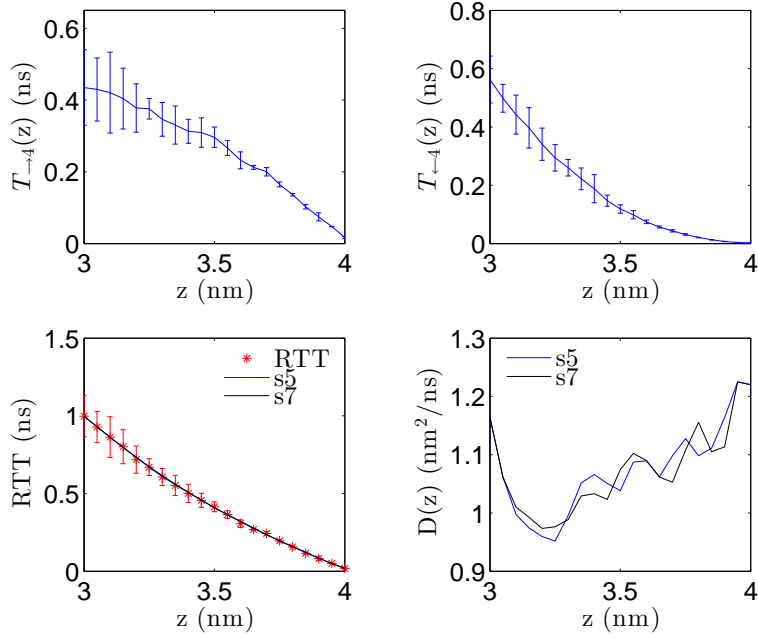


Figure 3.17: $T_{\rightarrow x}^{|ax>}(z)$, $T_{z\leftarrow}^{<zb|}(x)$, $T_{\rightleftarrows x}^{|ab|}(z)$ and diffusion profiles for region IV.

3.1.5 Permeation in Three Layers

As it was done for water previously [46], it is informative to study permeation of the molecule in step wise manner. This approach provides the insight of how different layers (hydrophobic and hydrophilic) of membrane structure affect insertion, translocation and dissociation processes of dyclonine. We set $z = -a$ nm and $z = a$ nm as interface of hydrophobic and hydrophilic regions for extracellular and intracellular leaflets, respectively.

As complete permeation process is the continuous steps of insertion, translocation and dissociation, we can split (3.3) as

$$R = \int_{-L}^{-a} dx \frac{e^{\Delta u(x)}}{D(x)} + \int_{-a}^a dx \frac{e^{\Delta u(x)}}{D(x)} + \int_a^L dx \frac{e^{\Delta u(x)}}{D(x)}. \quad (3.15)$$

Note that regions between $z = -L - z = -a$ and $z = a - z = L$ correspond to hydrophilic layers of membrane including lipid head groups and area between $z = -a - z = a$ corresponds to hydrophobic layer including lipid tails. Additionally, it is important to indicate that first and third terms in right hand side are equal to each other since $u(z) = u(-z)$ and $D(z) = D(-z)$ due to symmetric construction of the bilayer.

The first term in the right hand side represents the resistance of insertion process

$$R_i \equiv \int_{-L}^{-a} dx \frac{e^{\Delta u(x)}}{D(x)} \equiv \frac{1}{\mathcal{P}_i} \quad (3.16)$$

where \mathcal{P}_i is permeation coefficient of insertion. While the second term corresponds to resistance of translocation process, we need to make a correction here. As $\Delta u(x) = u(x) - u_{out}$ and we want to estimate permeation of translocation process it is needed to determine the $u(z) - u(-a)$ where $z = -a$ is the position where translocation starts. The second term at the right hand side of (3.15) is

$$R_t \equiv \int_{-a}^a dx \frac{e^{\Delta u(x)}}{D(x)}. \quad (3.17)$$

And when we introduce $e^{-u(-a)}e^{u(-a)}$, equation (3.17) yields

$$R_t \equiv \int_{-a}^a dx \frac{e^{u(x)-u_{out}+u(-a)-u(-a)}}{D(x)}, \quad (3.18)$$

which can be substituted as

$$R_t \equiv e^{-u_{out}}e^{u(-a)} \int_{-a}^a dx \frac{e^{u(x)-u(-a)}}{D(x)} \equiv \frac{1}{P\mathcal{P}_t}. \quad (3.19)$$

Note that $e^{-u_{out}}e^{u(-a)}$ is the ratio of number of molecules in water to number of molecules in lipid so we define partition coefficient P as $e^{-u(-a)}/e^{-u_{out}}$. Also, in that relation \mathcal{P}_t is the permeability coefficient of translocation process.

Similarly for the dissociation process, we can write

$$R_d \equiv \int_a^L dx \frac{e^{\Delta u(x)}}{D(x)} = e^{-u_{\text{out}}} e^{u_a} \int_a^L dx \frac{e^{u(x)-u(a)}}{D(x)} \equiv \frac{1}{P\mathcal{P}_d}, \quad (3.20)$$

where \mathcal{P}_d is the permeability coefficient of dissociation process.

As it was indicated before first and third term are equal to each other in relation (3.15),

$$\mathcal{P}_i = P\mathcal{P}_d, \quad (3.21)$$

and total resistance is

$$R = R_i + R_t + R_d, \quad (3.22)$$

which yields

$$\frac{1}{\mathcal{P}} = \frac{1}{\mathcal{P}_i} + \frac{1}{P\mathcal{P}_t} + \frac{1}{P\mathcal{P}_d}. \quad (3.23)$$

3.2 Results

3.2.1 Free Energy Profiles

Unrestrained Simulations

The probability distributions of the charged (Figure 2.7B) and neutral (Figures 2.13B and 2.18B) dyclonine molecules along the bilayer normal are proportional to Boltzmann factor of the free energy:

$$p(z) \propto e^{-\frac{G(z)}{k_B T}}. \quad (3.24)$$

Here $p(z)$ is the probability of being at location z , $G(z)$ is the free energy per mole at location z .

The free energy profiles of the systems $8D^+$, $8D^0$ and $4D^0$ deduced from equation (3.24) are shown in Figure 3.18. Note that energy profiles can be shifted in y axis since normalization is missing in equation (3.24). We see that charged molecules (black) encounter a slight barrier at around $z = 2.5$ nm and reach their minimum energy value at around $z = 1.9$ nm at just below of phosphorous atoms of phospholipids.

When we analyze the energy profiles of neutral systems, we see there is a high energy barrier at $z = 2$ nm for $8D^0$ system (dashed red). As neutral dyclonine molecules move as a cluster in water, this energy barrier is not for an individual dyclonine molecule, it is the energy barrier for accumulated dyclonine molecules. Because when they accumulate once, they almost never dissociate (Figure 2.16) and act as one bulky molecule. On the other hand, both neutral dyclonine systems ($4D^0$ solid red, $8D^0$ dashed red) provide a consistent profile inside of the bilayer that they have minimum at around $z = 1.1$ nm and do not fluctuate much at positions deeper than that location.

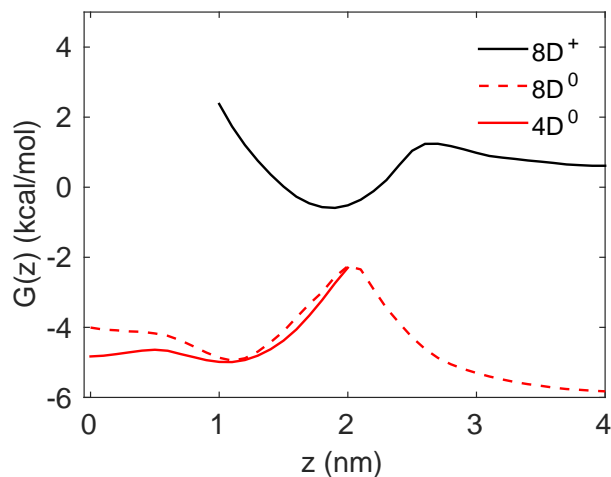


Figure 3.18: Free energy profiles obtained from position distributions of $8D^+$ (black solid line), $8D^0$ (red dashed line) and $4D^0$ (red solid line) systems are shown.

Although we are able to obtain energy profiles for charged and neutral dyclonine molecules, we can only have them partially. As we do not have energy values for charged one where $|z| < 1$ nm and $|z| > 2$ nm for neutral ones, we are unable to determine permeation with these profiles.

Restrained Simulations

Free energy profiles obtained by umbrella sampling simulations are shown in Figure 3.19 overlapped with profiles obtained from $8D^+$, $8D^0$ and $4D^0$ simulations. For neutral dyclonine (red), for the locations $|z| < 2$ nm we see that energy values obtained by umbrella sampling (dotted solid line) is consistent with the profiles obtained by $8D^0$ (dashed line) and $4D^0$ (solid line) systems. Similar with $8D^0$ and $4D^0$ energy profiles, neutral molecule prefers to stay around $z = 1.1$ nm. On the contrary of the profile obtained by $8D^0$ system simulations, we see no barrier while neutral dyclonine is penetrating into bilayer. This is expected because as it was mentioned before, the energy barrier seen for $8D^0$ system does not represent an individual molecule, but for a bulk composed of seven neutral dyclonines. We see that for neutral molecule locating around $z = 1.1$ nm is approximately 8 kcal/mol more favorable compared to outside of the bilayer. Since neutral dyclonine is a hydrophobic molecule this energy profile is an expected outcome.

Note that neutral dyclonine is initiated from 2.8 kcal/mol above of charged one in aqueous environment. The reason is the fact that charged dyclonine is found 10^{pK_a-pH} times more abundant than neutral one. Boltzmann distribution yields

$$\frac{p_{D^+}}{p_{D^0}} = \frac{e^{\frac{-G_{aq}^+(z)}{k_B T}}}{e^{\frac{-G_{aq}^0(z)}{k_B T}}} \quad (3.25)$$

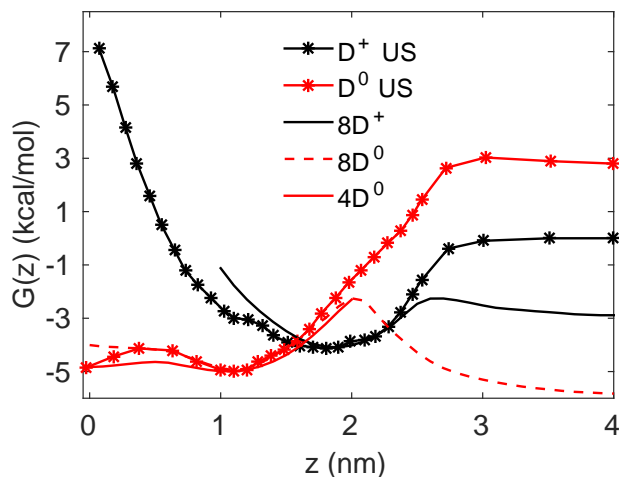


Figure 3.19: Free energy profiles obtained from umbrella sampling simulations for charged (dotted black) and neutral (dotted red) are shown overlapped with free energy profiles obtained by unrestrained $8D^+$ (black solid), $8D^0$ (red dashed) and $4D^0$ (red solid) simulations.

where $G_{aq}^+(z)$ is free energy of charged dyclonine in aqueous environment, $G_{aq}^0(z)$ is free energy of neutral dyclonine in aqueous environment and $\frac{p_{D^+}}{p_{D^0}}$ is the ratio of charged species to neutral ones which is equal to $10^{pK_a - pH}$. Therefore,

$$k_B T \ln[10^{(pK_a - pH)}] = -G_{aq}^{D^+}(z) + G_{aq}^{D^0}(z) \quad (3.26)$$

where $pK_a = 8.4$, $pH = 6.5$ and $T = 323$ K. Since we chose the energy value of charged dyclonine as zero in aqueous environment, energy of neutral dyclonine in aqueous environment was set as 2.8 kcal/mol.

When we examine the energy profiles of charged dyclonine (black), we see that energy profile obtained from umbrella sampling simulations are consistent for the 1.3 nm - 2.5 nm interval. It is hard to claim that it is also consistent for the interval of 1 nm - 1.3 nm, the reason may be the insufficient sampling of unrestrained simulations as charged dyclonine is not able to penetrate into the core of the membrane. In addition, we see a difference for the locations $|z| > 2.5$ nm. The reason is the simulation time of the unrestrained system. As simulation duration increases, the profile obtained from unrestrained simulations converges to the profile obtained from umbrella sampling simulations. In Figure 3.20, we see that when only 100 ns of the simulation is used we see a higher difference, whereas when we use 250 ns of simulations we see a closer profile.

As we force the charged molecule to locate in the core of the membrane, the energy barrier increases and reaches approximately 7 kcal/mol at the center of the bilayer. The reason is that while dyclonine is dragged into the core, water molecules and lipid head groups are also dragged with the charged head group of dyclonine. In Figure 3.21, we see that more than four phosphorous atoms are located in the core region (which is defined as the

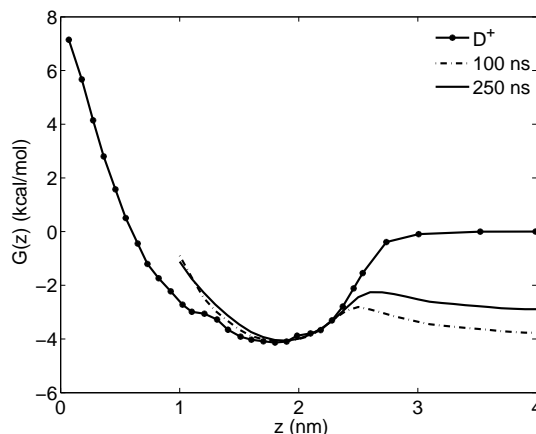


Figure 3.20: Increasing the simulation time from 100 ns (dotted dashed line) to 250 ns (solid line) provides more consistent profile with umbrella sampling simulations (dotted solid line).

area between $z = -1.3$ nm and $z = 1.3$ nm) of the membrane as the charged molecule is forced to locate inside of the membrane. On the other hand, number of phosphorous atoms do not increase with drift of neutral dyclonine through the inside of the membrane since it does not pull phosphorous atoms. Similar with phosphorous atoms, number of

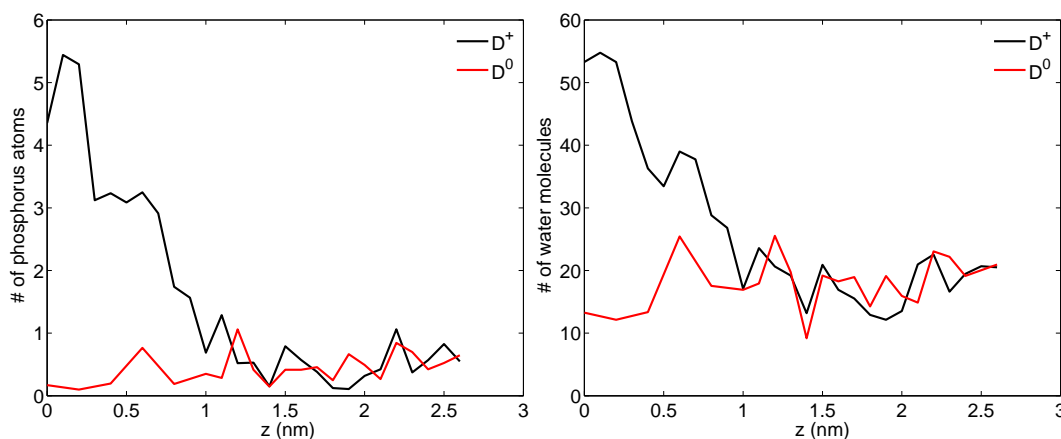


Figure 3.21: Number of phosphorous atoms can increase up to four when charged dyclonine is located in the core region (black) while no phosphorous atom is drifted into core region when neutral dyclonine is dragged into lipid core (red) (left). Number of water molecules increases up to 55 when charged dyclonine is located in the core region (black) while number of water molecules does not change no phosphorous atom is drifted into core region when neutral dyclonine is dragged into lipid core (red) (right).

water molecules increases as charged dyclonine approaches to the center of the bilayer. In Figure 3.21 at left, it is seen that number of water molecules in the lipid core reaches to 55 when charged dyclonine is forced to locate at the center (black), while the number of waters is similar when neutral dyclonine is located in aqueous environment and at the center of the membrane (red).

Views of the lipid bilayers for the umbrellas in which molecules are located at the center of the bilayer is shown in Figure 3.22. Phosphorous atoms (greenish brown) and water atoms (red) penetrate into bilayer when charged dyclonine is located at the center (left), while they do not invade when neutral dyclonine is located at the center (right).

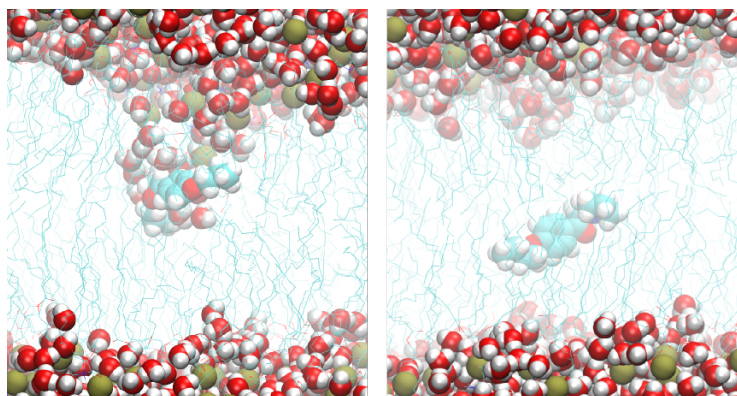


Figure 3.22: While charged dyclonine molecule cause deformation by dragging water molecules and lipid head groups, neutral dyclonine does not change the structure of the membrane.

3.2.2 Diffusion Profile

In this study, to calculate diffusion profile two approaches were used: global and local. As global approach round-trip time of the molecules between two virtual boundaries are estimated. As local approach pTCFs are used to determine diffusion coefficients.

Global estimate of diffusion profile

Diffusion profiles for all intervals are shown in Fig 3.23 (smoothing over seven points are used). Solid lines show the profile of the condition which absorbing boundary is greater than reflecting boundary and dashed lines show the profile of the condition which reflecting boundary is greater than absorbing boundary. Black lines shows the diffusion profiles determined from unrestrained simulations of charged dyclonine molecules and red lines shows the diffusion profiles determined from unrestrained simulations of neutral dyclonine molecules. It is seen that while diffusion is approximately $0.1 \text{ nm}^2/\text{ns}$ inside of the membrane, it is order of magnitude larger ($1.1 \text{ nm}^2/\text{ns}$) in aqueous environment.

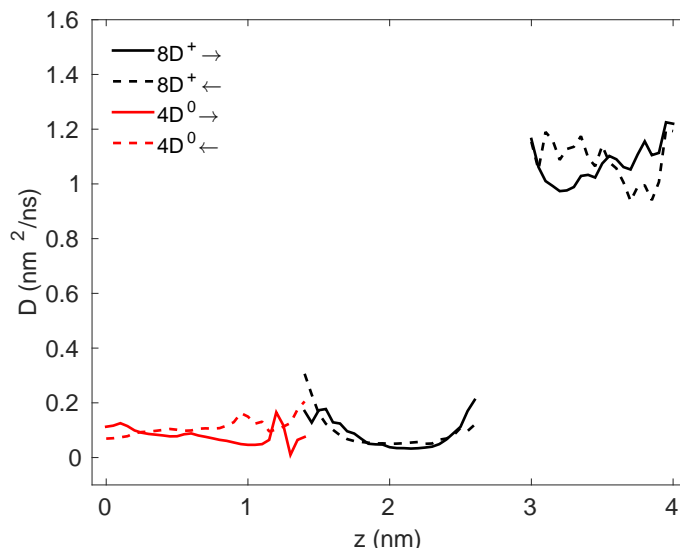


Figure 3.23: Diffusion profiles are shown for all regions. Solid lines show the ones whose absorbing boundary is greater than reflecting boundary, dashed lines show the ones whose absorbing boundary is smaller than reflecting boundary.

Local estimate of diffusion profile

Resulting local diffusion values for charged (black circles) and neutral (red circles) dyclonine molecules are shown in Figure 3.24. We can see that charged and neutral states of dyclonine have almost same diffusion values for the same positions. Moreover, it is seen that diffusion coefficients determined via pTCF are consistent with the profile obtained by round-trip time (Figure 3.24, black and red lines).

For simplicity, we fit the profiles to a hyperbolic tangent function (Figure 3.24, blue). In order to confirm fitted profile (hyperbolic tangent function) is realistic, round-trip time for the intervals are calculated and compared with the τ_{rt} determined from MD simulations.

In Figure 3.25, τ_{rt} from MD simulations and τ_{rt} estimated from fitted diffusion profiles for region I (up), region II (middle) and region IV (down) are shown for $\tau_{x \rightleftharpoons x}^{|ab|}(z)$ (left) and $\tau_{x \leftarrow x}^{|ab|}(z)$ (right). It is clear that with a few exception, calculated τ_{rt} from fitted diffusion profile is in the range of MD τ_{rt} deviation which proves fitted diffusion profile is successful in representing diffusion profile of the molecule in MD simulations.

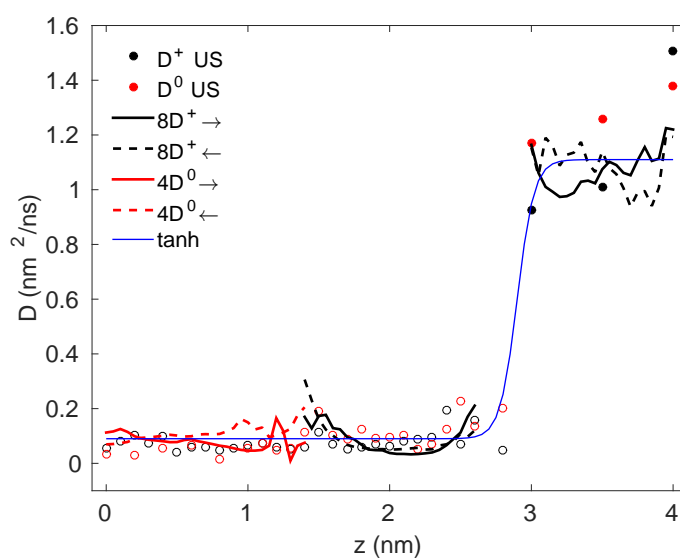


Figure 3.24: All diffusion profiles are shown determined via global approach (black and red lines) and local approach (black and red circles). Overall profile is fitted to hyperbolic tangent function (blue). Filled circles are the diffusion coefficients calculated from mono-exponential fits, empty circles are the diffusion coefficients calculated from biexponential functions.

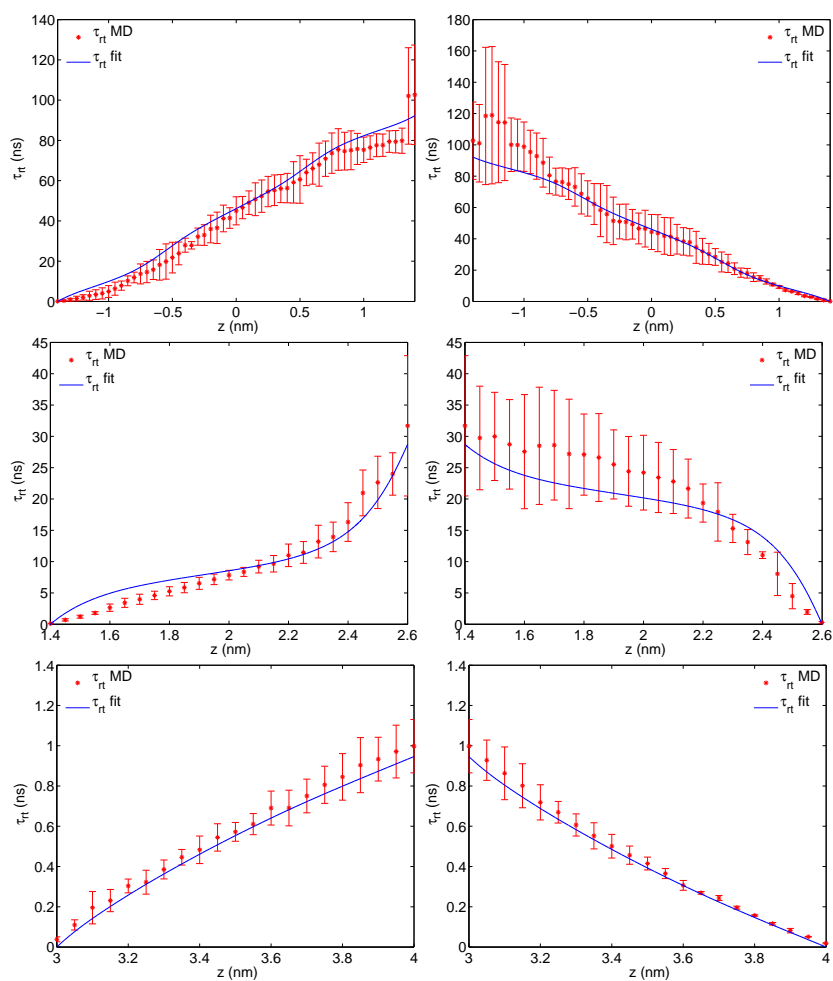


Figure 3.25: τ_{rt} calculated from fitted diffusion function consistent with τ_{rt} determined MD simulations for region I (up), region II (middle) and region IV (down) are shown for $\tau_{x \rightleftharpoons}^{|ab|}(z)$ (left) and $\tau_{\rightleftharpoons x}^{|ab|}(z)$ (right).

3.2.3 Permeation

Choice of border (L) for the calculations of permeation is arbitrary and one could wonder whether different choice of borders would effect the total permeability. In order to determine it we calculated overall permeations for $L = 3.5$ nm, $L = 4$ nm and $L = 4.5$ nm. Results are given in Table 3.3.

	$L = 3.5$ nm	$L = 4$ nm	$L = 4.5$ nm
D^+	1.2406×10^{-3}	1.2405×10^{-3}	1.2405×10^{-3}
D^0	29.73	23.15	19.16

Table 3.3: Calculated permeability coefficients (cm/s) for charged and neutral dyclonine with different choice of borders

It is seen that permeability coefficient of neutral molecule is approximately 10^4 times higher than charged molecule independent of border selection. Therefore, $L = 4$ nm will be studied from now on.

Calculated resistance values for insertion, translocation and dissociation processes for both states are given in Table 3.4.

	$1/P_i$	$1/P_t$	$1/P_d$	$\log P$	$1/P$
D^+	1.65 ns	35.86 ms	733.39 ns	2.6482	80.61 μs
D^0	2.16 ns	20.96 ns	113.14 μs	4.7193	4.32 ns

Table 3.4: Calculated “resistances” (per nm) to the insertion into, translocation through, and dissociation from a DPPC lipid bilayer. Together with $\log P$, these give the total “resistance” $1/P$. ($a = 1.5$ nm and $L = 4$ nm.)

When we look the rates of insertion process, it is seen the resistance for both molecules are approximately same which indicates charge state does not affect penetration of the molecule into bilayer. On the other hand when we examine the translocation rates of both states the effect of charge is seen clearly that translocation of neutral molecule is approximately six order of magnitude faster than charged one. Lastly, in dissociation process rate of charged dyclonine is approximately 150 times higher than neutral. Actually here we see the effect of partition coefficient. Since neutral molecule prefers to stay at $z = a$ $10^{4.7193}/10^{2.6482}$ times more than charged one, it encounters higher resistance during dissociation.

Overall resistance of bilayer to charged molecule is approximately 20000 times higher compared to neutral one which is the result of dominance of translocation process.

3.3 Discussion

Free energies determined from unrestrained and restrained simulations provide consistent profiles with exceptions of entrance the neutral and charged molecule. The difference of neutral dyclonine is caused by the accumulation of molecules in water in unrestrained simulations which act as a bulky molecule. And the difference of charged dyclonine is caused by sampling size. As the duration of unrestrained simulations increase, free energy profile converges to umbrella sampling profile.

In order to be able to permeate the bilayer, charged dyclonine needs to overcome a high energy barrier (~ 7 kcal/mol), while neutral molecule does not encounter any energy barrier. This situation is plausible since charged molecule deforms the membrane by pulling phosphate groups and water molecules into the core of the bilayer which does not occur for neutral molecule. Similar behaviors of ionizable basic species are reported. For example, adamantanes (which are used for treatment of Parkinson's Disease) encounter a high energy barrier (> 10 kcal/mol) in their protonated state while they do not face a energy barrier in their neutral state [47]. In another study which focuses on amitriptyline (which is an antidepressant), it is shown that molecule has an energy value of ~ 4 kcal/mol in the center of the membrane while it is ~ -6 kcal/mol for neutral state [37]. Moreover there are other researches that study local anesthetic molecules. However, they only analyze the molecules in their neutral state. For example, benzocaine can face a slight energy barrier of ~ 4 kcal/mol with respect to minimum energy value along the bilayer normal which is around $z = 1.1$ nm similar to dyclonine [13]. They also study this molecule with two sets of atomic partial charge which cause a shift in local minima of energy profile ~ 2.5 kcal/mol while it does not change position of the minimum value besides the difference of energy at the center compared to minimum value.

As we used in this research, it is possible to use both local and global approaches to determine diffusion profile of the molecule since they provide consistent results. On the other hand, both methodologies have some limitations. While using round-trip time provides plausible and consistent results within the chosen virtual boundaries, complete profile cannot be determined with this approach since we do not have any molecule that leaves lipid bilayer within the simulation time. Meanwhile, using pTCF as local approach provides a complete profile since we use umbrella sampling simulations to determine it. However, some pTCFs are not successful in decaying to zero which changes the diffusion coefficient in corresponding position (Converging to zero for pTCFs is important because otherwise the area under the curve of the function increases resulting order of magnitude smaller diffusion coefficient). In order to eliminate this issue, parameters of fit are restricted which caused relatively less successful fits. Since we calculate diffusion coefficients from these fits, dissonance of the pTCF and fit affects reliability of the calculated coefficients. But for a specific position resulting coefficient with restrictions are

more consistent with the coefficient calculated via round-trip time. Overall, it is possible to indicate that although both approaches have some limitations, consistent results for complete profile is obtained with some corrections.

For diffusion profiles we can conclude that charged and neutral state have almost same diffusion coefficient for a specific position and diffusion coefficient in aqueous environment is approximately one order of magnitude greater than the value inside of the membrane. This outcomes are consistent with the studies for other molecules. For aspirin and ibuprofen (which are acidic drugs have antiinflammatory effect), it is reported that diffusion inside of the membrane is $\sim 0.2 \times 10^{-5}$ cm²/s and it is order of magnitude larger in water while the values are independent of charged state [25]. Additionally, in another research that studies tyramine (which is a basic drug used as a neuroregulator) has a diffusion coefficient around 0.7×10^{-5} cm²/s in aqueous environment which is approximately 5 times higher than the coefficients inside of the bilayer [33].

Studying permeation of the molecule with three-layer view provides detailed information of characteristic behaviors of insertion, translocation and dissociation processes. It is shown that while insertion process is completed within the same time scale, translocation of charged dyclonine lasts $\sim 10^6$ times longer compared to neutral one. In addition, dissociation of neutral molecule is completed ~ 150 times slower than charged one. This results show us, the ratio of charged dyclonine permeability coefficient to neutral dyclonine (which is $\sim 10^4$) is dominated by translocation process which is slightly recovered by dissociation process while insertion process do not lead and contribution in terms of the ratio.

It is important to remind that these resistance values are actually depended on the type of phospholipids of the bilayer. It is plausible to think that the choice of chain length and saturation state can affect the transition rate whereas type of head group may impact insertion and dissociation rates. One would expect shorter chain would increase the translocation rate resulting higher permeability coefficient. Mathai et al. studies water permeation with different lipid types. For example, in that study permeability coefficients of water through DMPC and DLPC bilayers (whose thicknesses are 2.54 nm and 2.09 nm, respectively) are reported as 8.3×10^{-3} cm/s and 10.4×10^{-3} cm/s, respectively. As the only difference between these two lipid types is the number of carbon atoms in lipid tail (14 and 12, respectively) it is clear smaller chain length increases permeability coefficient as rate of translocation increases. In a recent study, researchers wanted to see whether different head groups with the same chain length and saturation state affect the permeability of a drug, norfloxacin (which is an antibacterial drug) or not[48]. For this purpose, they compared the permeabilities of DOPC vs DOPE:DOPC (3:7) and DOPC vs DOPG:DOPC (3:7) membranes. The only difference between phospholipid types (DOPC, DOPE and DOPG) is their head group. DOPC has a cholin group and phosphate group (net charge is zero), DOPE has amine group instead of cholin group resulting smaller head group

(net charge is zero). On the other hand, DOPG is an anionic lipid. As a result of first experimental condition, they see that permeability of the neutral norfloxacin decreases with introducing of DOPC since it compacts the head groups of the lipids which obstructs entrance of the drug into hydrophobic core. As second experimental condition, introducing anionic lipids DOPG also compacts phospholipids via forming hydrogen bonding with neighboring phospholipids. It is indicated that, this situation blocks entrance of the neutral molecule, again resulting a decrease in permeability coefficients. Therefore, it is necessary to emphasize that selection of phospholipids are critical for permeation studies which directly effects the calculated value.

Chapter 4

Modeling Experimental Studies in Drug Permeation

4.1 Introduction

In addition to computational studies, there are many experimental studies focus on determination of permeability coefficients of drugs and other molecules [48, 49, 50, 51, 52, 53]. One method to measure the permeability of proton is using markers as fluorescence which are sensitive to change in pH [54]. Eyer et al. studied permeation of ionizable basic drugs through liposomal membrane with fluorescence assay and emphasize that it is the first method that uses fluorescence as pH indicator for measurement of drug permeabilites [55].

For this purpose they develop a fluorescence array. Basically, they generate liposomes composed of POPC and load fluorescence dye into these vesicles. This fluorescence dye is pH sensitive and as pH changes in the range of 6 - 9, fluorescence signal increases linearly. In that study they aim to measure permeability coefficient of basic drugs (that are all aliphatic amine bearing drugs). In their system as a neutral drug enters into the liposome and grabs a proton, pH of the environment rises. This leads to an increase in fluorescence signal which would be a measure of drug permeation.

In the first 0.5 s of their measurement, they obtain a biexponentially increasing function and they fit to the relation,

$$F = Ae^{-k_a t} + Be^{-k_b t} + F_0, \quad (4.1)$$

where F is the fluorescence signal, k_a and k_b are rates, A and B are corresponding weighting functions and F_0 is the coefficient to arrange the starting value.

Permeation rate of a molecule is determined via

$$k_a = \mathcal{P}_{app} \frac{A_v}{V_v}, \quad (4.2)$$

$$k_{D^+} = \mathcal{P}_{D^+} \frac{A_v}{V_v}, \quad (4.3)$$

$$k_{D^0} = \mathcal{P}_{D^0} \frac{A_v}{V_v}, \quad (4.4)$$

$$k_{H^+} = \mathcal{P}_{H^+} \frac{A_v}{V_v}, \quad (4.5)$$

where \mathcal{P}_{app} is the permeability coefficient of the molecule, A_v is area and V_v is volume of the vesicle. Therefore, rate can be calculated as,

$$\mathcal{P}_{app} = k_a \frac{r}{3}, \quad (4.6)$$

where r is the radius of the liposome.

One assumption to calculate \mathcal{P}_{app} from charged and neutral species is,

$$\mathcal{P}_{app} = f_{D^+} \mathcal{P}_{D^+} + f_{D^0} \mathcal{P}_{D^0}, \quad (4.7)$$

where f_{D^+} and f_{D^0} are fractions, \mathcal{P}_{D^+} and \mathcal{P}_{D^0} are permeability coefficients of charged and neutral drugs, respectively. Note that for the conditions where $\mathcal{P}_{D^+} \ll \mathcal{P}_{D^0}$ first term in the right hand side of the equation (4.7) can be ignored. This leads to determination of \mathcal{P}_{D^0} via

$$\mathcal{P}_{D^0} = \mathcal{P}_{app} (1 + 10^{\text{pK}_a - \text{pH}}), \quad (4.8)$$

where $f_{D^0} = 1/(1 + 10^{\text{pK}_a - \text{pH}})$. Therefore in that research they indicate it is possible to determine apparent permeability of the drug via fluorescence signal and this provides to determine permeability coefficient of neutral state of the studied drugs.

For the same system, they also measure the fluorescence signal for 500 s. In long scale, the signal of the fluorescence molecule decays. They fit the long scale profile to four exponential function,

$$F = Ae^{-k_a t} + Be^{-k_b t} + Ce^{-k_c t} + De^{-k_d t} + F_0. \quad (4.9)$$

Fitted coefficients of equation (4.1) to fluorescence signal of propranolol (whose parameters are used for modeling) is given in Table 4.1 ([55], Supplementary Table 1) .

Note that signs of A and B are negative, indicating ascending phases; C and D are positive, indicating descending phases of the exponential function.

By using equation (4.6), \mathcal{P}_{app} can be calculated as $1.95 \times 10^{-4} \text{ cm s}^{-1}$ where $k_a = 66.5 \text{ s}^{-1}$ and $r = 87.5 \text{ nm}$. Permeability of neutral state can be estimated via equation (4.8) 0.77 cm s^{-1} where $\text{pH}=5.9$ and $\text{pK}_a=9.5$. In the paper they report $\mathcal{P}_{app} = 3.89 \times 10^{-4} \text{ cm}$

A	k_a (s ⁻¹)	B	k_b (s ⁻¹)	C	k_c (s ⁻¹)	D	k_d (s ⁻¹)
-0.116	66.7	-0.0326	17.5	0.0379	0.0418	0.0677	0.00319

Table 4.1: Coefficients of fitted four exponential function to fluorescence signal of propranolol.

s⁻¹ and permeability coefficient of neutral species as 1.55 cm s⁻¹.

4.2 Methods

For the modeling, experimental values of propranolol are used [55].



where D^+ , D^0 are charged and neutral states of the drug and H^+ is proton. k_{on} and k_{off} are association and dissociation rates, respectively.

Meanwhile note that

$$\frac{k_{off}}{k_{on}} = \frac{[D^0]_{eq}[H^+]_{eq}}{[D^+]_{eq}} = K_a, \quad (4.11)$$

where K_a is acid dissociation constant and remember $pK_a = -\log(K_a)$. Therefore,

$$k_{off}/k_{on} = 10^{-pK_a}. \quad (4.12)$$

In order to calculate pH change in the vesicle, rate equations of $[D_i^+]$, $[D_i^0]$ and $[H_i^+]$ are written for charged, neutral drugs and proton, respectively.

Initial values for the modeling is given in Table 4.2.

Concentration	Value	Concentration	Value
$[H_o^+]$	10^{-pH} M	$[H_i^+]_{t=0}$	10^{-pH} M
$[D_o^+]$	10 μ M	$[D_i^+]_{t=0}$	0
$[D_o^0]$	$[D_o^+](10^{pH-pK_a})$ μ M	$[D_i^0]_{t=0}$	0
$[Na_o^+]$	0.2 M	$[Na_i^+]_{t=0}$	0.2 M
$[Cl_o^-]$	0.2 M	$[Cl_i^-]_{t=0}$	0.2 M
Permeability Coefficient	Value	Protonation Rate	Value
\mathcal{P}_{H^+}	10^{-7} cm s ⁻¹	k_{on}	10^{10} M ⁻¹ s ⁻¹
\mathcal{P}_{D^+}	1.55×10^{-4} cm s ⁻¹	k_{on}^F	10^9 M ⁻¹ s ⁻¹
\mathcal{P}_{D^0}	1.55 cm s ⁻¹		
\mathcal{P}_{Na^+}	10^{-14} cm s ⁻¹		
\mathcal{P}_{Cl^-}	10^{-11} cm s ⁻¹		

Table 4.2: Parameters used in the model.

Outside concentration of species are assumed constant and k_{off} values are determined via equation (4.12). \mathcal{P}_{D^0} is taken as $\mathcal{P}_{D^+} \times 10^{-4}$ since 10^{-4} is the ratio of permeability coefficient of charged dyclonine to neutral dyclonine that we determined in previous chapter.

The change of $[D^+]$, $[H^+]$ and $[D^0]$ in the vesicle can be written as

$$\frac{d}{dt}[H_i^+] = -k_{on}[D_i^0][H_i^+] + k_{off}[D_i^+] + k_{H^+}\Delta c_{H^+}, \quad (4.13)$$

$$\frac{d}{dt}[D_i^0] = -k_{on}[D_i^0][H_i^+] + k_{off}[D_i^+] + k_{D^0}\Delta c_{D^0}, \quad (4.14)$$

and

$$\frac{d}{dt}[D_i^+] = k_{on}[D_i^0][H_i^+] - k_{off}[D_i^+] + k_{D^+}\Delta c_{D^+}. \quad (4.15)$$

Note that first and second terms in the right hand side of equations (4.13), (4.14) and (4.15) represent switch between two states of the molecule based on equation (4.10) and the third term is the contribution of permeation. Here, Δc_{H^+} , Δc_{D^+} and Δc_{D^0} are concentration difference between outside and inside ($\Delta c = c_{out} - c_{in}$) of the vesicle for proton, charged and neutral drug, respectively. k_{H^+} , k_{D^+} and k_{D^0} are permeation rates of the proton, charged and neutral drug, respectively.

Model 1a As first step, lets assume only neutral dyclonine can permeate the bilayer. The permeability of charged molecule is ignored since, at least for our case, permeability coefficient of charged drug is approximately 10^{-4} times smaller than the neutral one. (Permeation of proton is not introduced since its permeability is even smaller than charged drug [56]). So third terms in equations of (4.13) and (4.15) drop.

Model 1b Since there are also fluorescence molecules in liposomes which are also protonable (for HPTS $pK_a=8.5$ [9]), it is expected to see an effect of the fluorophore on pH profile in the vesicle.



where k_{on}^F and k_{off}^F are association and dissociation rates of fluorophore.

Therefore change of fluorophore concentration with time can be written as

$$\frac{d}{dt}[F^0] = k_{on}^F[F^-][H^+] - k_{off}^F[F^0] \quad (4.17)$$

and

$$\frac{d}{dt}[\text{F}^-] = -k_{on}^{\text{F}}[\text{F}^-][\text{H}^+] + k_{off}^{\text{F}}[\text{F}^0]. \quad (4.18)$$

Note that there is no term for permeation through bilayer since molecules are unable to permeate.

Obviously, it will affect proton concentration with an addition to the equation (4.13). Resulting rate equation of proton is

$$\frac{d}{dt}[\text{H}_i^+] = -k_{on}[\text{D}_i^0][\text{H}_i^+] + k_{off}[\text{D}_i^+] - k_{on}^{\text{F}}[\text{F}^-][\text{H}^+] + k_{off}^{\text{F}}[\text{F}^0] + k_{H^+}\Delta c_{H^+}. \quad (4.19)$$

Model 2a In *model 1*, we assumed permeation of charged drug has no effect on pH since its permeation is too slow. In this model, the third term in equation (4.15) is introduced.

Model 2b Introducing permeation of charged drug changed pH profile (see Results), resulting a different curve from experimental data ([55] Figure 2b). Since membrane potential may be the factor blocks permeation of charged species into the bilayer, it is introduced into the model.

The current carried by an ion S can be calculated via multiplying permeability, \mathcal{P}_S , with nonlinear function of voltage. Goldman-Hodgkin-Katz (GHK) current equation [57, 58] yields,

$$I_S = \mathcal{P}_S z_S \frac{VF}{RT} \frac{[\text{S}_i] - [\text{S}_o] \exp(-z_S FV/RT)}{1 - \exp(-z_S FV/RT)}, \quad (4.20)$$

where z_S is charge of S, R and F are gas and Faraday constants, T is temperature. And V is the membrane potential which is denoted in GHK voltage equation

$$V = \frac{RT}{F} \ln \left(\frac{\sum \mathcal{P}_c[\text{cation}_o] + \sum \mathcal{P}_a[\text{anion}_i]}{\sum \mathcal{P}_c[\text{cation}_i] + \sum \mathcal{P}_a[\text{anion}_o]} \right), \quad (4.21)$$

where $[\text{cation}_o]$, $[\text{cation}_i]$, $[\text{anion}_o]$ and $[\text{anion}_i]$ are concentrations of cations and anions at outside and inside of the vesicle, respectively. \mathcal{P}_c and \mathcal{P}_a are permeability coefficients of cations and anions in the system.

By implementation of membrane potential into rate equations of charged dyclonine and proton (equations (4.15) and (4.19)) gives

$$\frac{d}{dt}[\text{D}_i^+] = k_{on}[\text{D}_i^0][\text{H}_i^+] - k_{off}[\text{D}_i^+] + k_{D^+} V \frac{[\text{D}_o^+]e^{-V} - [\text{D}_i^+]}{1 - e^{-V}} \quad (4.22)$$

and

$$\frac{d}{dt}[\text{H}_i^+] = -k_{on}[\text{D}_i^0][\text{H}_i^+] + k_{off}[\text{D}_i^+][\text{H}_i^+] - k_{on}^F[\text{F}^-][\text{H}^+] + k_{off}^F[\text{F}^0] + k_{H^+}V \frac{[\text{H}_o^+]e^{-V} - [\text{H}_i^+]}{1 - e^{-V}}, \quad (4.23)$$

where

$$V = \ln \left(\frac{\mathcal{P}_{D^+}[\text{D}_o^+] + \mathcal{P}_{H^+}[\text{H}_o^+]}{\mathcal{P}_{D^+}[\text{D}_i^+] + \mathcal{P}_{H^+}[\text{H}_i^+]} \right). \quad (4.24)$$

Note that RT/F in calculation of potential, V , will be canceled when it is implemented in the current equation. Therefore they are not rewritten in equations (4.22), (4.23) and (4.24) for simplicity.

Model 3 As system also includes Cl^- and Na^+ ions, they are also introduced into the system. Ion concentration is 20 mM in the studied experiment, so initial concentrations of ions in the vesicle were set to 20 mM ($[\text{Na}_i^+]_{t=0} = 20$ mM, $[\text{Cl}_i^-]_{t=0} = 20$ mM) and outside ion concentrations were kept constant ($[\text{Na}_o^+] = 20$ mM, $[\text{Cl}_o^-] = 20$ mM).

Since the membrane potential is effected when ions are introduced into the system, voltage should be expressed as

$$V = \ln \left(\frac{\mathcal{P}_{D^+}[\text{D}_o^+] + \mathcal{P}_{H^+}[\text{H}_o^+] + \mathcal{P}_{\text{Na}^+}[\text{Na}_o^+] + \mathcal{P}_{\text{Cl}^-}[\text{Cl}_i^-]}{\mathcal{P}_{D^+}[\text{D}_i^+] + \mathcal{P}_{H^+}[\text{H}_i^+] + \mathcal{P}_{\text{Na}^+}[\text{Na}_i^+] + \mathcal{P}_{\text{Cl}^-}[\text{Cl}_o^-]} \right). \quad (4.25)$$

Rate equations of charged dyclonine and proton are same with equations (4.22) and (4.23) with modified voltage expression (4.25). And as Na^+ and Cl^- ions are capable of permeate the bilayer even though their permeability coefficients are extremely low, we write rate equations of ions inside of the membrane as

$$\frac{d}{dt}[\text{Na}_i^+] = k_{\text{Na}^+}V \frac{[\text{Na}_o^+]e^{-V} - [\text{Na}_i^+]}{1 - e^{-V}} \quad (4.26)$$

and

$$\frac{d}{dt}[\text{Cl}_i^-] = k_{\text{Cl}^-}(-V) \frac{[\text{Cl}_o^-]e^V - [\text{Cl}_i^-]}{1 - e^V}, \quad (4.27)$$

where k_{Na^+} and k_{Cl^-} are permeability rates of Na^+ and Cl^- ions calculated via (4.5) where $\mathcal{P}_{\text{Na}^+}$ and $\mathcal{P}_{\text{Cl}^-}$ are permeability coefficients which are taken as 10^{-14} cm s⁻¹ and 10^{-11} cm s⁻¹, respectively [59].

4.3 Results

First, initial 0.5 s of pH profile was analyzed via the models that are explained above.

Model 1a As initial model, there are only proton, charged and neutral drugs present in the vesicle and only neutral drug can permeate through bilayer. In Figure 4.1, we see that

within 0.2 s pH reaches equilibrium.

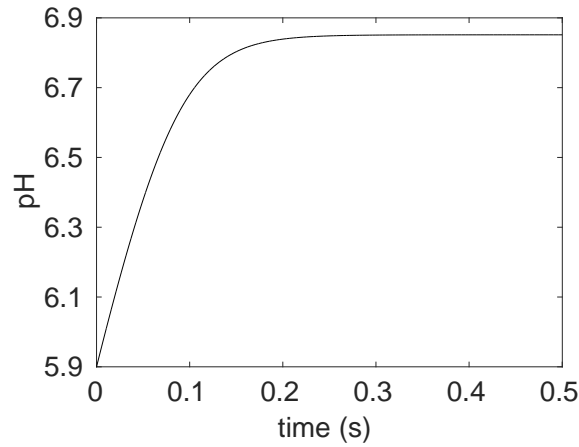


Figure 4.1: pH increases with time and saturates around $t = 0.2$ s which is consistent with experimental data.

Figure 4.2 shows that concentration of charged drug is also saturated within 0.2 s and neutral drug is saturated in $10 \mu\text{s}$.

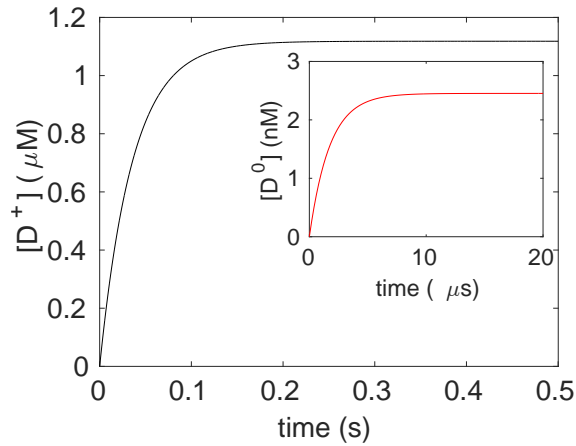


Figure 4.2: Charged (black), neutral (red, inset) drug concentration change over time. Note that neutral dyclonine concentration reach to equilibrium in $10 \mu\text{s}$.

As equilibration of neutral drug occurs in μs scale, it is plausible to keep $[D_i^0] = [D_o^0]$ which effects equilibration of neither pH nor charged drug (Figure 4.3).

For this system, rate equations for $[D_i^+]$ and $[H_i^+]$ can be written as

$$\begin{bmatrix} [D_i^+] \\ [H_i^+] \end{bmatrix} = \begin{bmatrix} -k_{off} & k_{on}[D_i^0] \\ k_{off} & -k_{on}[D_i^0] \end{bmatrix} \begin{bmatrix} [D_i^+] \\ [H_i^+] \end{bmatrix},$$

Eigenfunction of the matrix is $(1, -1)$ and corresponding eigenvalue is $-(k_{off} + k_{on}[D_i^0])$ that gives the rate of exponential function.

In addition, it is also possible to predict weighting coefficient of exponential function (A), which is the saturation point of $[D_i^+]$. Note that in the equation (4.10), $[D_i^+] = 0$,

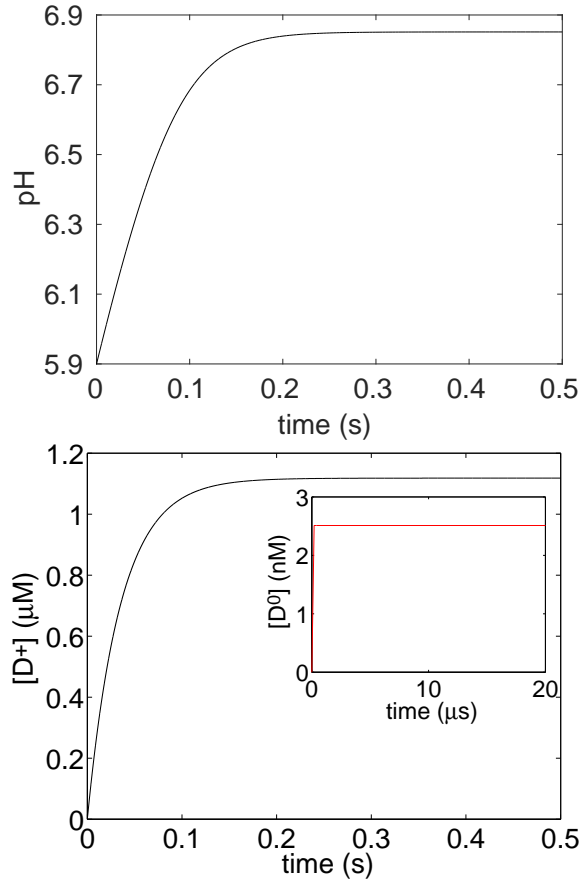


Figure 4.3: pH and neutral drug concentration profiles when neutral drug concentration is kept constant

$[D_i^0] = [D_o^0]$ which is constant and $[H_i^+] = 10^{-pH}$ at $t = 0$. At equilibration, $[D_i^+]_{eq} = x$, $[D_i^0]_{eq} = [D_o^0]$ and $[H_i^+]_{eq} = 10^{-pH} - x$ where x is the saturation concentration of charged drug. As,

$$K_d = \frac{[D_i^0]_{eq}[H_i^+]_{eq}}{[D_i^+]_{eq}} = \frac{[D_o^0][10^{-pH} - x]}{x} \quad (4.28)$$

resulting,

$$x = 10^{-pH}[D_o^0]/(K_d + [D_o^0]). \quad (4.29)$$

So as we know both rate, $k_a = k_{on}[D^0] + k_{off}$, and weighting value, $A = x = 10^{-pH}[D_o^0]/(K_d + [D_o^0])$ we are supposed to predict pH change over time.

Model 1b Note that this is a monoexponential function which is not consistent with experimental results reported in the study of Eyer et al.[55]. There is also a fluorescence molecule (HPTS) in the vesicle which has an ionizable side chain at $pK_a = 8.5$. Hence, we introduced the fluorescence molecule into the systems as described in the equations (4.17), (4.18) and (4.19). Resulting change in the pH is shown in the Figure 4.4.

Here it is seen that there is a second time scale (which is not detected in Figure 4.1)

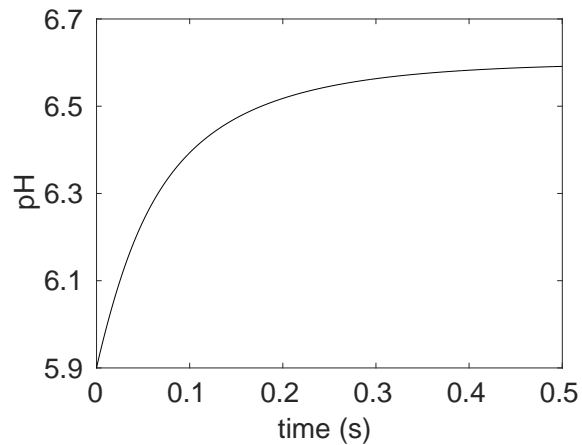


Figure 4.4: Fluorescence molecule introduces the second exponent in pH profile.

as a result of contribution of the fluorescence molecule.

Model 2a In order to see whether permeation of charged drug affects the internal pH, we simulated the system after letting charged molecule and proton penetration into the vesicle. Resulting system is shown in Figure 4.5.

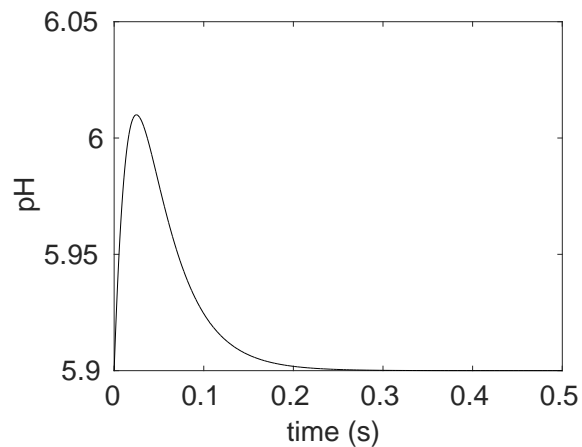


Figure 4.5: pH decreases back to its initial value in a short time when charged drug and proton permeabilities are introduced to the system.

As it is seen in the figure, introducing the charged drug permeation into the system provides reaching back to the initial pH value in a short time. The reason is when charged drugs are internalized into vesicle they become a proton source to the vesicle which provides recovery of the initial pH in just 0.2 s. Note that since the vesicle size is extremely small, given pH corresponds to only a few H^+ ions. That is why the pH inside of the vesicle is highly sensitive to permeation of charged drug. On the other hand, proton permeability does not effect the result (data not shown) since both its permeability and concentration are too small that can be said within the studied time scale it is difficult for a proton to enter into vesicle.

Model 2b As pH profile of the previous model is not consistent with experimental pH profile, some other property should be added to the model which can inhibit internalization of charged drug. For this purpose, membrane potential was introduced to the *model 2a*. Resulting pH profile is shown in Figure 4.6.

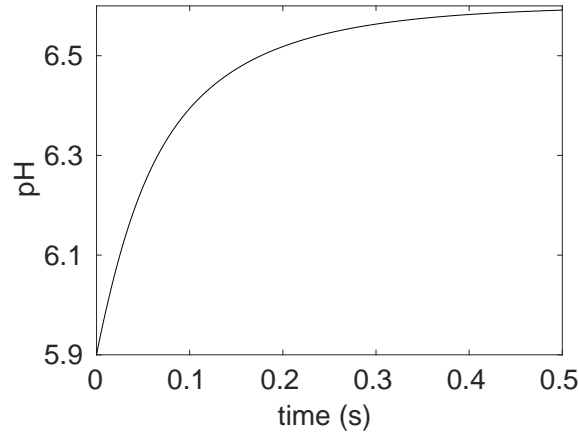


Figure 4.6: Membrane potential blocks permeation of charged drug which provides achieving experimental results.

It is seen that introducing membrane potential blocks recovery of pH resulting pH profile consistent with experimental pH profile.

Model 3 Since the medium of the experiment includes ions, Na^+ and Cl^- ion permeabilities were added to the simulation which may have effect on membrane potential. Resulting pH profile is shown in Figure 4.7.

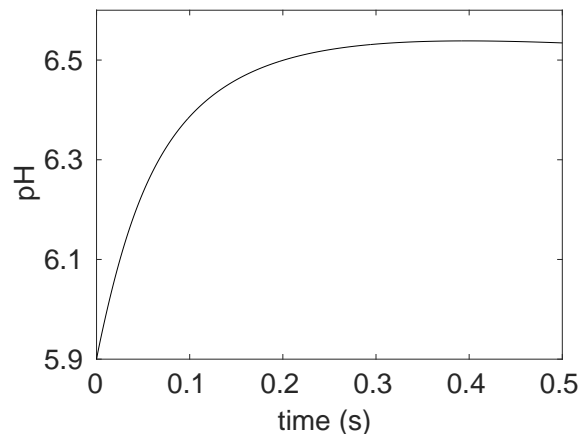


Figure 4.7: Addition of ions into the system changes the pH profile via changing membrane potential.

Although it is difficult to distinguish Figure 4.7 from Figure 4.6, when pH profiles are fit to equation (4.1), coefficients of the fits are changed (data not shown).

As the researchers indicate by determining the fastest rate of exponential function, k_a , it is possible to determine permeability coefficient. However as we show in the *model 1a*, the rate is only dependent on k_{on} and $[D_i^0]$. When \mathcal{P}_{D^0} is multiplied and divided by three, resulting fit parameters are given in 4.3.

\mathcal{P}_{D^0} (cm s ⁻¹)	A	k_a (s ⁻¹)	B	k_b (s ⁻¹)	\mathcal{P}_{app} (cm s ⁻¹)	\mathcal{P}_{D^0} (cm s ⁻¹)
0.52	-0.060	28.72	-0.581	12.99	0.84×10^{-4}	0.33
1.55	-0.068	31.19	-0.57	13.18	0.91×10^{-4}	0.36
4.65	-0.066	33.09	-0.57	13.28	0.96×10^{-4}	0.38

Table 4.3: Coefficients of biexponential fits to simulations of different \mathcal{P}_{D^0} . \mathcal{P}_{app} values were calculated via equation (4.6) and \mathcal{P}_{D^0} values were calculated via equation (4.8).

Note that when we change the permeability coefficient of neutral drug on the order of magnitude, calculated \mathcal{P}_{app} (and so \mathcal{P}_{D^0}) via equation (4.6) does not change linearly. Therefore, this experimental approach to determine permeability coefficients should be open to discussion.

On the other hand, as we change k_{on} , k_a also changes. The change of the pH profile is shown in Figure 4.8. Resulting coefficients are given in Table 4.4. As it is seen in table, there is a linear relation with k_{on} and k_a .

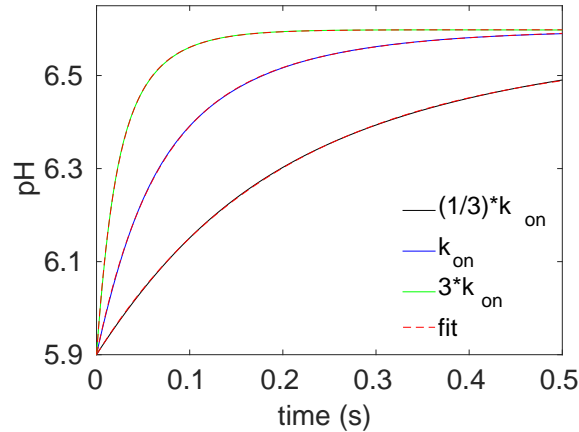


Figure 4.8: Change of k_{on} affects k_a linearly.

k_{on} (M ⁻¹ s ⁻¹)	A	k_a (1/s)	b	k_B (1/s)
$1/3 \times 10^{10}$	-0.188	7.14	-0.470	3.99
10^{10}	-0.415	18.53	-0.285	6.840
3×10^{10}	-0.384	56.87	-0.31	21.56

Table 4.4: Coefficients of biexponential fits to simulations of different k_{on} .

As it is seen changing k_{on} affects the k_a linearly. Ion concentrations are different from previous analysis. Because for this k_{on} analysis, higher values result a slight decay which will be discussed below.

In the article, authors indicate they also analyze the fluorescence signal for longer times and fit to four-exponential function which is stated in equation (4.9).

We simulated *model 2b* for 500 s, resulting pH profiles are shown in the Figure 4.9.

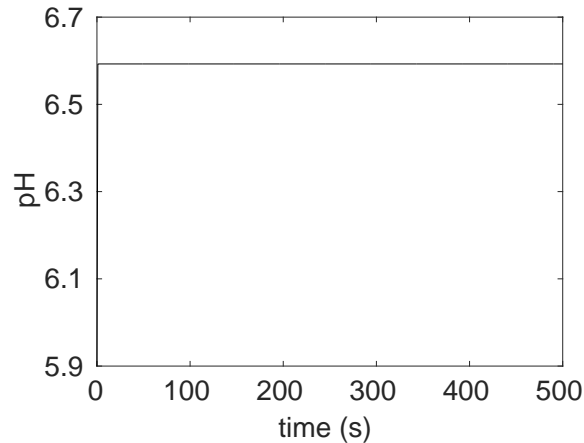


Figure 4.9: When ions are not introduced into the system *model 2b*, pH never decreases back to its initial value on the contrary of the experimental outcome.

It is seen that when ions are not in the system, pH in the vesicle remains constant. Additionally, we simulated *model 3* for 500 s with different ion permeability coefficients (black and blue) and fit it to four-exponential functions (red dashed).

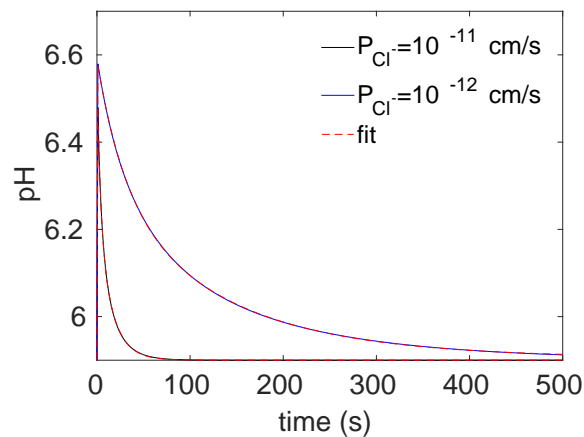


Figure 4.10: When pH profile is analyzed for longer time, it is seen that permeability coefficients of ions are important in descending phase of exponential function. Changing permeability coefficient of Cl^- ion order of magnitude affects pH profile drastically.

It is seen that for longer times, pH is recovered and reached back the initial value. Coefficients of descending exponents of the four exponential functions changes as the permeability coefficients of ions are changed. This shows that descending phases of pH

profile in long time scale is dependent on ion permeability. In the article, it is stated that pH recovery may be the result of proton leakage into the vesicle. However, changing proton permeability does not differ obtained coefficients of last two exponents of fit function.

4.4 Discussion

In this chapter, we constructed a kinetic model with an increasing complexity to study an experimental method which aims to measure permeability coefficients of some basic ionizable drugs. It is shown that fastest rate of biexponential function does not report permeability of the molecule. While it is almost non-sensitive to change in permeability coefficient of the drug, it can be claimed that this phase is highly sensitive to protonation rate, k_{on} , of the drug. Moreover, it is possible to calculate k_{on} with our simplest model, *model 1a*.

Meanwhile, it seen that since the chosen fluorescence molecule is also ionizable, its presence affects the pH profile that interferes with effect of the drug. This situation results the second exponent on the pH profile in short term (0.5 s) (*model 1b*). Since it is not as easy to determine k_{on} as in the *model 1a*, chose of another fluorescence molecule which is not ionizable could lead to determine k_{on} of ionizable drugs with this experimental method.

Additionally, we show that the reason of not seeing the effect of charged state is not because its permeability coefficient is too small to permeate the bilayer in short time, but it is the membrane potential which blocks permeation of charged species (*model 2a, model 2b*).

Since ions are also present in the medium, it is studied whether introducing them into the simulation would effect the pH profile in the liposome. Even though effects of ions are barely noticeable in short term (0.5 s), it is obvious that their permeabilities have dominant effects on the pH profile in descending phases of the pH profile (500 s). It seems that it may be possible to determine permeability coefficients of ions with the information of descending phase rates (*model 3*).

Overall it is hard to confirm the apparent permeability coefficients of drugs that are determined with this experimental model are the “real” values of permeabilities. In our simulations, we see that change in permeability coefficients of neither charged nor neutral states are effective in changing any rate of the exponents. In addition to drug permeabilities, proton permeability also fails to lead any difference in rates.

Chapter 5

Conclusion and Outlook

5.1 Conclusion

In this research, it was aimed to understand the permeability mechanism of an aliphatic amine bearing drug, dyclonine, and its permeation through the lipid bilayer in atomistic detail via molecular dynamics simulations. Since drugs which have aliphatic amines constitute the largest subgroup of all drugs, revealing detailed information about drug-lipid interaction and permeability of dyclonine is expected to provide insight about permeation of many other drugs.

In second chapter, MD studies showed that dyclonine has different characteristic properties in both charge states. While both of the states were capable of entering into bilayer spontaneously, only neutral drug was able to change leaflet. It was observed that during entrance into the bilayer, molecule should approach with a specific orientation in order to be able to succeed in insertion process, otherwise drug could penetrate into bilayer partially and left the membrane in a few seconds. After insertion process was completed, charged molecules failed to change leaflet because of the hydrophobic core of the membrane. Once charged dyclonine entered into bilayer, it adhered its protonated part to phosphate groups of phospholipid via electrostatic interactions and did not penetrate into the bilayer core. On the other hand, once neutral dyclonine entered into bilayer it is translocated several times without preferring any specific location along bilayer normal.

In third chapter, permeability coefficients of both charge states were calculated. For this purpose, we needed to construct free energy and diffusion profiles along the bilayer normal. Complete profiles of free energy of both states were obtained via umbrella sampling simulations. As charged dyclonine deformed membrane by drifting phosphate groups and water molecules to the bilayer core, energy cost of locating the charged state increased at the center of the membrane. On the other hand, molecule in neutral state preferred to locate in the core of membrane.

Using two approaches to determine diffusion profile revealed consistent profiles. It

was shown that both states have approximately same diffusion coefficient for each location along the lipid bilayer normal. Overall profiles showed that diffusion coefficients inside of the membrane is one order of magnitude lower compared to aqueous environment.

Permeation of the molecules were studied with three-layer perspective in order to understand how different structural compositions of bilayer impact permeation of the drug. Since phospholipids have polar and non-polar regions, bilayer can be separated into three layers with a non-polar region restricted by two polar layers. As molecules behave completely different in polar and non-polar regions based on their structure and physicochemical properties, studying the permeation in three-layer view provided characteristics of both charged states of the drug in different environments. We showed that while insertion of both neutral and protonated dyclonine have same rate in insertion, the effect of charge appears during translocation process. While neutral dyclonine can change leaflet in nanoseconds, charged dyclonine is capable of completing this process in milliseconds. In the dissociation step, it is seen that charged molecule is slightly faster than neutral one. Overall, we saw that while neutral dyclonine is rather fast in permeation, charged dyclonine is approximately 10^{-4} times slower.

Although there is no experimental study for determination of dyclonine permeability, many other drugs are studied to measure their permeabilities via various experimental techniques. One of these methods is the usage of pH sensitive markers as fluorescence molecules. A recent study [55], focuses on permeability of aliphatic amine bearing drugs and design liposomal fluorescence assay to measure permeabilities of a couple of drugs. Kinetic models with increasing complexity were constructed to study this experimental system in chapter 4. Results indicate that the parameter that they suggest as the “measure” of the permeability is actually sensitive to proton binding rate rather than drug permeabilities on the contrary of their claim. With a few modification to current system, it may be possible to determine protonation rates of drugs and maybe permeability coefficients of ions.

Overall, in this thesis we study drug permeation from atomistic detail to kinetic models. With these methodologies we are able to show characteristic behaviors of drug-lipid interactions, determine permeability coefficients of a drug for both charged states and model one of the experimental methods to determine drug permeability. The results we obtained may be used to design new drugs and experimental techniques to determine permeabilities.

5.2 Outlook

In this study we focused on the mechanism of aliphatic amine bearing drugs, using the same method one can study the second largest group of drugs, carboxylic acid bearing

drugs.

Since liposomal fluorescence assay is not the unique method to measure permeabilities of drugs, other methods can be modeled in order to understand their success in measurement of the permeabilities.

Additionally, as the initial motivation was the “promiscuous synergism” of pentamidine, MD simulations can be performed to understand pentamidine-lipid interaction and permeation through lipid bilayer. Actually, we had already started MD simulations of pentamidine and preliminary studies show that when they span the membrane, they change the thickness of it. However, it should be understood how pentamidine spans the membrane and what is the energy cost for it. Therefore umbrella sampling simulations can be performed for pentamidine.

Bibliography

- [1] D. S. Wishart, C. Knox, A. C. Guo, S. Shrivastava, M. Hassanali, P. Stothard, Z. Chang, and J. Woolsey, “DrugBank: a comprehensive resource for in silico drug discovery and exploration.,” *Nucleic acids research*, vol. 34, no. Database issue, pp. D668–D672, 2006.
- [2] T. Huang, B. J. Barclay, T. I. Kalman, R. C. Von Borstel, and P. J. Hastings, “The phenotype of a dihydrofolate reductase mutant of *Saccharomyces cerevisiae*,” *Gene*, vol. 121, pp. 167–171, 1992.
- [3] M. Cokol, H. N. Chua, M. Tasan, B. Mutlu, Z. B. Weinstein, Y. Suzuki, M. E. Nergiz, M. Costanzo, A. Baryshnikova, G. Giaever, C. Nislow, C. L. Myers, B. J. Andrews, C. Boone, and F. P. Roth, “Systematic exploration of synergistic drug pairs,” *Molecular Systems Biology*, vol. 7, no. 1, 2011.
- [4] C. Lipinski, F. Lombardo, B. Dominy, and P. Feeney, “Experimental and Computational Approaches to Estimate Solubility and Permeability in Drug Discovery and Development Settings,” *Advanced Drug Delivery Reviews*, vol. 23, pp. 3–25, 1997.
- [5] P. Norvaisas and A. Ziemys, “The role of payload hydrophobicity in nanotherapeutic pharmacokinetics,” *Journal of Pharmaceutical Sciences*, vol. 103, no. 7, pp. 2147–2156, 2014.
- [6] K. Yilancioglu, Z. B. Weinstein, C. Meydan, A. Akhmetov, I. Toprak, A. Durmaz, I. Iossifov, H. Kazan, F. P. Roth, and M. Cokol, “Target-independent prediction of drug synergies using only drug lipophilicity,” *Journal of Chemical Information and Modeling*, vol. 54, no. 8, pp. 2286–2293, 2014.
- [7] D. T. Manallack, R. J. Prankerd, G. C. Nassta, O. Ursu, T. I. Oprea, and D. K. Chalmers, “A Chemogenomic Analysis of Ionization Constants-Implications for Drug Discovery,” *ChemMedChem*, vol. 8, no. 2, pp. 242–255, 2013.
- [8] D. T. Manallack, M. L. Dennis, M. R. Kelly, R. J. Prankerd, E. Yuriev, and D. K. Chalmers, “The Acid/Base Profile of the Human Metabolome and Natural Products,” *Molecular Informatics*, vol. 32, no. 5-6, pp. 505–515, 2013.

-
- [9] “chemicalize.org was used for dyclonine to obtain logD property, 2015, chemicalize.org and ChemAxon (<http://www.chemaxon.com>).”
`\url{http://www.chemicalize.org/structure/#!mol=dyclonine&source=fp}`.
- [10] H. J. Florestano and M. E. Bahler, “Antimicrobial properties of dyclonine hydrochloride, a new topical anesthetic,” *Journal of the American Pharmaceutical Association*, vol. 45, no. 5, pp. 320–325, 1956.
- [11] M. D. L. C. Harris Jr., M. D. J. C. Parry, and M. D. F. E. Greifenstein, “DYCLONINEA NEW LOCAL ANESTHETIC AGENTCLINICAL EVALUATION,” *Anesthesiology*, vol. 17, no. 5, pp. 648–652, 1956.
- [12] R. Pérez-Isidoro, F. J. Sierra-Valdez, and J. C. Ruiz-Suárez, “Anesthetic diffusion through lipid membranes depends on the protonation rate.” 2014.
- [13] L. J. Martin, R. Chao, and B. Corry, “Molecular dynamics simulation of the partitioning of benzocaine and phenytoin into a lipid bilayer,” *Biophysical Chemistry*, vol. 185, pp. 98–107, 2014.
- [14] C. J. Hogberg, A. Maliniak, and A. P. Lyubartsev, “Dynamical and structural properties of charged and uncharged lidocaine in a lipid bilayer,” *Biophysical Chemistry*, vol. 125, no. 2-3, pp. 416–424, 2007.
- [15] E. H. Mojumdar and A. P. Lyubartsev, “Molecular dynamics simulations of local anesthetic articaine in a lipid bilayer,” *Biophysical Chemistry*, vol. 153, no. 1, pp. 27–35, 2010.
- [16] a. D. Mackerell, Jr, D. Bashford, M. Bellott, R. L. Dunbrack, J. D. Evanseck, M. J. Field, S. Fischer, J. Gao, H. Guo, S. Ha, D. Joseph-McCarthy, L. Kuchnir, K. Kuczera, F. T. K. Lau, C. Mattos, S. Michnick, T. Ngo, D. T. Nguyen, B. Prodhom, W. E. Reiher, Iii, B. Roux, M. Schlenkrich, J. C. Smith, R. Stote, J. Straub, M. Watanabe, J. W. Rkiewicz-Kuczera, D. Yin, and M. Karplus, “All-Atom Empirical Potential for Molecular Modeling and Dynamics Studies of Proteins,” *J Phys Chem B*, vol. 102, no. 97, pp. 3586–3616, 1998.
- [17] A. D. MacKerell, M. Feig, and C. L. Brooks, “Improved Treatment of the Protein Backbone in Empirical Force Fields,” *Journal of the American Chemical Society*, vol. 126, no. 3, pp. 698–699, 2004.
- [18] J. B. Klauda, R. M. Venable, J. A. Freites, J. W. O’Connor, D. J. Tobias, C. Mondragon-Ramirez, I. Vorobyov, A. D. MacKerell, and R. W. Pastor, “Update of the CHARMM All-Atom Additive Force Field for Lipids: Validation on Six Lipid Types,” *Journal of Physical Chemistry B*, vol. 114, no. 23, pp. 7830–7843, 2010.

-
- [19] M. J. Frisch, G. W. Trucks, H. B. Schlegel, G. E. Scuseria, M. A. Robb, J. R. Cheeseman, G. Scalmani, V. Barone, B. Mennucci, G. A. Petersson, H. Nakatsuji, M. Caricato, X. Li, H. P. Hratchian, A. F. Izmaylov, J. Bloino, G. Zheng, J. L. Sonnenberg, M. Hada, M. Ehara, K. Toyota, R. Fukuda, J. Hasegawa, M. Ishida, T. Nakajima, Y. Honda, O. Kitao, H. Nakai, T. Vreven, J. A. Montgomery Jr., J. E. Peralta, F. Ogliaro, M. Bearpark, J. J. Heyd, E. Brothers, K. N. Kudin, V. N. Staroverov, R. Kobayashi, J. Normand, K. Raghavachari, A. Rendell, J. C. Burant, S. S. Iyengar, J. Tomasi, M. Cossi, N. Rega, J. M. Millam, M. Klene, J. E. Knox, J. B. Cross, V. Bakken, C. Adamo, J. Jaramillo, R. Gomperts, R. E. Stratmann, O. Yazyev, A. J. Austin, R. Cammi, C. Pomelli, J. W. Ochterski, R. L. Martin, K. Morokuma, V. G. Zakrzewski, G. A. Voth, P. Salvador, J. J. Dannenberg, S. Dapprich, A. D. Daniels, Ö. Farkas, J. B. Foresman, J. V. Ortiz, J. Cioslowski, and D. J. Fox, "Gaussian09 {R}evision {D}.01."
- [20] S. Jo, T. Kim, V. G. Iyer, and W. Im, "CHARMM-GUI: A web-based graphical user interface for CHARMM," *Journal of Computational Chemistry*, vol. 29, no. 11, pp. 1859–1865, 2008.
- [21] J. C. Phillips, R. Braun, W. Wang, J. Gumbart, E. Tajkorsid, E. Villa, C. Chipot, R. D. Skeel, L. Kale, and K. Schulten, "Scalable molecular dynamics with {NAMD}," *J. Comp. Chem.*, vol. 26, pp. 1781–1802, 2005.
- [22] A. Khajeh and H. Modarress, "Effect of cholesterol on behavior of 5-fluorouracil (5-FU) in a DMPC lipid bilayer, a molecular dynamics study," *Biophysical Chemistry*, vol. 187-188, pp. 43–50, 2014.
- [23] M. Kang and S. M. Loverde, "Molecular Simulation of the Concentration-Dependent Interaction of Hydrophobic Drugs with Model Cellular Membranes," *The Journal of Physical Chemistry B*, vol. 118, no. 41, pp. 11965–11972, 2014.
- [24] A. Yousefpour, S. Amjad Iranagh, Y. Nademi, and H. Modarress, "Molecular dynamics simulation of nonsteroidal antiinflammatory drugs, naproxen and relafen, in a lipid bilayer membrane," *International Journal of Quantum Chemistry*, vol. 113, no. 15, pp. 1919–1930, 2013.
- [25] M. B. Boggara and R. Krishnamoorti, "Partitioning of nonsteroidal antiinflammatory drugs in lipid membranes: A molecular dynamics simulation study," *Biophysical Journal*, vol. 98, no. 4, pp. 586–595, 2010.
- [26] B. Van Oosten, D. Marquardt, I. Komljenović, J. P. Bradshaw, E. Sternin, and T. A. Harroun, "Small molecule interaction with lipid bilayers: A molecular dynamics study of chlorhexidine," *Journal of Molecular Graphics and Modelling*, vol. 48, pp. 96–104, 2014.

-
- [27] J. Ulander and A. D. J. Haymet, "Permeation across hydrated DPPC lipid bilayers: simulation of the titrable amphiphilic drug valproic acid.," *Biophysical journal*, vol. 85, no. 6, pp. 3475–3484, 2003.
- [28] M. Casalegno, G. Raos, and G. Sello, "Hydrophobic aggregation and collective absorption of dioxin into lipid membranes: insights from atomistic simulations," *Phys. Chem. Chem. Phys.*, vol. 17, no. 4, pp. 2344–2348, 2015.
- [29] S. Riahi and C. N. Rowley, "Why Can Hydrogen Sulfide Permeate Cell Membranes?," *Journal of the American Chemical Society*, vol. 136, no. 43, pp. 15111–15113, 2014.
- [30] D. Bemporad, and Jonathan W. Essex*, and C. Luttmann, "Permeation of Small Molecules through a Lipid Bilayer: A Computer Simulation Study," *The Journal of Physical Chemistry B*, vol. 108, no. 15, pp. 4875–4884, 2004.
- [31] L. Li, I. Vorobyov, and T. W. Allen, "The different interactions of lysine and arginine side chains with lipid membranes," *Journal of Physical Chemistry B*, vol. 117, no. 40, pp. 11906–11920, 2013.
- [32] D. Bonhenry, M. Tarek, and F. Dehez, "Effects of phospholipid composition on the transfer of a small cationic peptide across a model biological membrane," *Journal of Chemical Theory and Computation*, vol. 9, no. 12, pp. 5675–5684, 2013.
- [33] B. W. Holland, M. D. Berry, C. G. Gray, and B. Tomberli, "A Permeability Study of O_2 and the Trace Amine *p*-Tyramine through Model Phosphatidylcholine Bilayers," *PLoS ONE*, vol. 10, no. 6, p. e0122468, 2015.
- [34] A. E. Cardenas, R. Shrestha, L. J. Webb, and R. Elber, "Membrane Permeation of a Peptide: It Is Better to be Positive," *The Journal of Physical Chemistry B*, vol. 119, no. 21, pp. 6412–6420, 2015.
- [35] M. Paloncayova, R. Devane, B. Murch, K. Berka, and M. Otyepka, "Amphiphilic drug-like molecules accumulate in a membrane below the head group region," *Journal of Physical Chemistry B*, vol. 118, no. 4, pp. 1030–1039, 2014.
- [36] M. B. Boggara, M. Mihailescu, and R. Krishnamoorti, "Structural association of nonsteroidal anti-inflammatory drugs with lipid membranes," *Journal of the American Chemical Society*, vol. 134, no. 48, pp. 19669–19676, 2012.
- [37] J. Ma, L. Domicевичa, J. R. Schnell, and P. C. Biggin, "Position and orientational preferences of drug-like compounds in lipid membranes: a computational and NMR approach," *Phys Chem Chem Phys*, vol. 17, no. 30, pp. 19766–19776, 2015.

-
- [38] S. Amjad-Iranagh, A. Yousefpour, P. Haghighi, and H. Modarress, “Effects of protein binding on a lipid bilayer containing local anesthetic articaine, and the potential of mean force calculation: A molecular dynamics simulation approach,” *Journal of Molecular Modeling*, vol. 19, no. 9, pp. 3831–3842, 2013.
- [39] S.-J. Marrink and H. J. C. Berendsen, “Simulation of water transport through a lipid membrane,” *Journal of Physical Chemistry*, vol. 98, no. 15, pp. 4155–4168, 1994.
- [40] M. Souaille and B. Roux, “Extension to the weighted histogram analysis method: Combining umbrella sampling with free energy calculations,” *Computer Physics Communications*, vol. 135, no. 1, pp. 40–57, 2001.
- [41] S. Kumar, J. M. Rosenberg, D. Bouzida, R. H. Swendsen, and P. A. Kollman, “THE weighted histogram analysis method for free-energy calculations on biomolecules. I. The method,” *Journal of Computational Chemistry*, vol. 13, no. 8, pp. 1011–1021, 1992.
- [42] C. H. Bennett, “Efficient estimation of free energy differences from Monte Carlo data,” *Journal of Computational Physics*, vol. 22, no. 2, pp. 245–268, 1976.
- [43] G. Hummer, “Position-dependent diffusion coefficients and free energies from Bayesian analysis of equilibrium and replica molecular dynamics simulations,” *New Journal of Physics*, vol. 7, no. 1, p. 34, 2005.
- [44] C. Gardiner, *Stochastic Methods: A Handbook for the Natural and Social Sciences*. 2009.
- [45] Y. Von Hansen, S. Gekle, and R. R. Netz, “Anomalous anisotropic diffusion dynamics of hydration water at lipid membranes,” *Physical Review Letters*, vol. 111, no. 11, 2013.
- [46] J. C. Mathai, S. Tristram-Nagle, J. F. Nagle, and M. L. Zeidel, “Structural determinants of water permeability through the lipid membrane.,” *The Journal of general physiology*, vol. 131, no. 1, pp. 69–76, 2008.
- [47] C. F. Chew, A. Guy, and P. C. Biggin, “Distribution and dynamics of adamantanes in a lipid bilayer,” *Biophys. J.*, vol. 95, no. December, pp. 5627–5636, 2008.
- [48] S. Purushothaman, J. Cama, and U. Keyser, “Dependence of norfloxacin diffusion across bilayers on lipid composition,” *Soft Matter*, 2015.
- [49] J. M. A. Grime, M. A. Edwards, N. C. Rudd, and P. R. Unwin, “Quantitative visualization of passive transport across bilayer lipid membranes.,” *Proceedings of the National Academy of Sciences of the United States of America*, vol. 105, no. 38, pp. 14277–82, 2008.

-
- [50] S. Li, P. C. Hu, and N. Malmstadt, "Imaging molecular transport across lipid bilayers," *Biophysical Journal*, vol. 101, no. 3, pp. 700–708, 2011.
- [51] H. Jespersen, J. H. Andersen, H. J. Ditzel, and O. G. Mouritsen, "Lipids, curvature stress, and the action of lipid prodrugs: Free fatty acids and lysolipid enhancement of drug transport across liposomal membranes," *Biochimie*, vol. 94, no. 1, pp. 2–10, 2012.
- [52] A. V. Thomae, H. Wunderli-Allenspach, and S. D. Krämer, "Permeation of aromatic carboxylic acids across lipid bilayers: the pH-partition hypothesis revisited.," *Biophysical journal*, vol. 89, no. 3, pp. 1802–11, 2005.
- [53] T. Shimanouchi, H. Ishii, N. Yoshimoto, H. Umakoshi, and R. Kuboi, "Calcein permeation across phosphatidylcholine bilayer membrane: Effects of membrane fluidity, liposome size, and immobilization," *Colloids and Surfaces B: Biointerfaces*, vol. 73, no. 1, pp. 156–160, 2009.
- [54] C. L. Kuyper, J. S. Kuo, S. A. Mutch, and D. T. Chiu, "Proton permeation into single vesicles occurs via a sequential two-step mechanism and is heterogeneous," *Journal of the American Chemical Society*, vol. 128, no. 10, pp. 3233–3240, 2006.
- [55] K. Eyer, F. Paech, F. Schuler, P. Kuhn, R. Kissner, S. Belli, P. S. Dittrich, and S. D. Krämer, "A liposomal fluorescence assay to study permeation kinetics of drug-like weak bases across the lipid bilayer," *Journal of Controlled Release*, vol. 173, no. 1, pp. 102–109, 2014.
- [56] J. Zeng, K. E. Smith, and P. L. Chong, "Effects of alcohol-induced lipid interdigitation on proton permeability in L-alpha-dipalmitoylphosphatidylcholine vesicles.," *Biophysical journal*, vol. 65, no. 4, pp. 1404–14, 1993.
- [57] D. E. Goldman, "POTENTIAL, IMPEDANCE, AND RECTIFICATION IN MEMBRANES," *The Journal of General Physiology*, vol. 27, no. 1, pp. 37–60, 1943.
- [58] B. K. A L Hodgkin, "The effect of sodium ions on the electrical activity of the giant axon of the squid," *The Journal of Physiology*, vol. 108, no. 1, p. 37, 1949.
- [59] I. Vorobyov, T. E. Olson, J. H. Kim, R. E. Koeppe, O. S. Andersen, and T. W. Allen, "Ion-induced defect permeation of lipid membranes," *Biophysical Journal*, vol. 106, no. 3, pp. 586–597, 2014.